iScience

CellPress

Article

Electric-Field-Induced Connectivity Switching in Single-Molecule Junctions

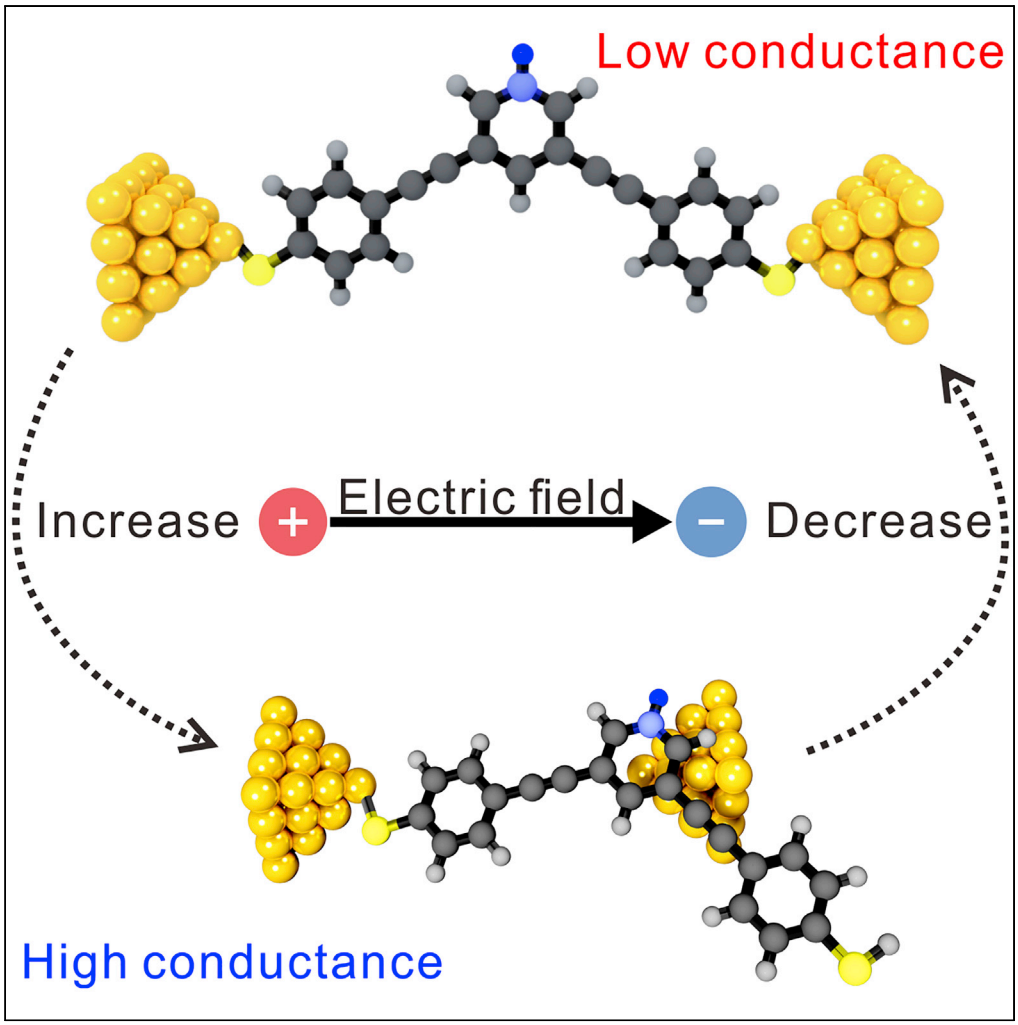

Chun Tang, Jueting Zheng, Yiling Ye, ..., Jia Shi, Haiping Xia, Wenjing Hong

whong@xmu.edu.cn (W.H.)
hpxia@xmu.edu.cn (H.X.)

HIGHLIGHTS

A strategy to *in-situ* switch the connectivity of single-molecule junctions

A concept to manipulate the molecule-electrode interaction

A molecular switch triggered by the varying of electric field

Experiments were combined with calculations to probe the switching mechanism

Tang et al., iScience *23*, 100770
January 24, 2020
https://doi.org/10.1016/j.isci.2019.100770

iScience

CellPress

Article

Electric-Field-Induced Connectivity Switching in Single-Molecule Junctions

Chun Tang,[1] Jueting Zheng,[1] Yiling Ye,[1] Junyang Liu,[1] Lijue Chen,[1] Zhewei Yan,[1] Zhixin Chen,[1] Lichuan Chen,[1] Xiaoyan Huang,[1] Jie Bai,[1] Zhaobin Chen,[1] Jia Shi,[1] Haiping Xia,[1,*] and Wenjing Hong[1,2,*]

SUMMARY

The manipulation of molecule-electrode interaction is essential for the fabrication of molecular devices and determines the connectivity from electrodes to molecular components. Although the connectivity of molecular devices could be controlled by molecular design to place anchor groups in different positions of molecule backbones, the reversible switching of such connectivities remains challenging. Here, we develop an electric-field-induced strategy to switch the connectivity of single-molecule junctions reversibly, leading to the manipulation of different connectivities in the same molecular backbone. Our results offer a new concept of single-molecule manipulation and provide a feasible strategy to regulate molecule-electrode interaction.

INTRODUCTION

The interaction between molecular components and electrodes is of fundamental importance to fabricate molecular devices (Hines et al., 2013; Moth-Poulsen and Bjørnholm, 2009; Ratner, 2013; Su et al., 2016; Xiang et al., 2016a). Pre-setting anchor groups (such as pyridine and thiol) in molecular backbones is one of the most typical strategies to manipulate the molecule-electrode interaction, which links the molecules to electrodes in designed connectivity (Leary et al., 2015). The connectivity of molecular devices determines not only the pathways of charge transport through molecule backbones but also the electronic properties of the molecule devices (Lambert, 2015; Liu et al., 2019). Such as the benzene in *meta*- and *para*-connectivity shows different types of quantum interference, which leads to significantly different conductance (Agraït et al., 2003; Aradhya et al., 2012b; Arroyo et al., 2013; Bai et al., 2019; Ballmann et al., 2012; Carlotti et al., 2018; Darwish et al., 2012; Frisenda et al., 2016; Garner et al., 2018; Guedon et al., 2012; Li et al., 2017, 2019; Liu et al., 2019; Mayor et al., 2003; Solomon et al., 2010; Su et al., 2016; Tang et al., 2019; Thompson and Nijhuis, 2016; Xiang et al., 2016a; Yoshizawa et al., 2008). The connectivity of single-molecule junctions can also determine the coupling site from the electrode to the molecule component, which has been utilized to construct a molecular switch by mechanical control (Aradhya et al., 2012a; Meisner et al., 2012; Quek et al., 2009). Moreover, such connectivity can regulate the coupling between electrodes and functional units of molecular components, which is essential for the design of molecular devices (Chen et al., 2017; Mayor et al., 2003; Xiang et al., 2016b). Because of the importance of connectivity in molecule devices, intensive efforts have been paid to construct stable and specific connectivity, whereas the manipulation of such connectivity in the same molecule backbone remained technically challenging. However, the efforts to reversibly tune the connectivity in the same molecular backbone would arouse new strategy to regulate the molecule-electrode interaction and lead to molecular devices with unique performances.

Recently, external electric field (EEF) has been proved to be a powerful tool to alter charge state (Koren et al., 2016), rupture chemical bonds (Zhang et al., 2018), vary molecule conformations (Bi et al., 2018; Gerhard et al., 2017; Lörtscher et al., 2006; Meded et al., 2009; Meng et al., 2019; Olavarria-Contreras et al., 2018), and even catalyze chemical reactions at the single-molecule scale (Aragonès et al., 2016; Ciampi et al., 2018; Huang et al., 2019; Shaik et al., 2016, 2018; Wang et al., 2018). The interaction between molecular components and EEF is based on the dipole-dipole interaction. Thus the tuning of such interaction provides the opportunity to regulate the favorable connectivity of single-molecule junctions in a neat and reversible way. To achieve such a goal, we choose pyridine as the functional building block. Pyridine can be protonated with significantly enhanced dipole moments (Figure 1B), which would prefer to reorient itself to counteract EEF, with the increasing trend to form an antiparallel arrangement when the strength of EEF increased (Figure 1C) (Brooke et al., 2018; Fujii et al., 2015; Li et al., 2016; Vergeer et al., 2006). Meanwhile, pyridine also has the binary interaction with electrodes by the ring coupling or the lone pair

[1]State Key Laboratory of Physical Chemistry of Solid Surfaces, College of Chemistry and Chemical Engineering, Collaborative Innovation Center of Chemistry for Energy Materials, Xiamen University, 361005 Xiamen, China

[2]Lead Contact

*Correspondence: whong@xmu.edu.cn (W.H.), hpxia@xmu.edu.cn (H.X.)

https://doi.org/10.1016/j.isci.2019.100770

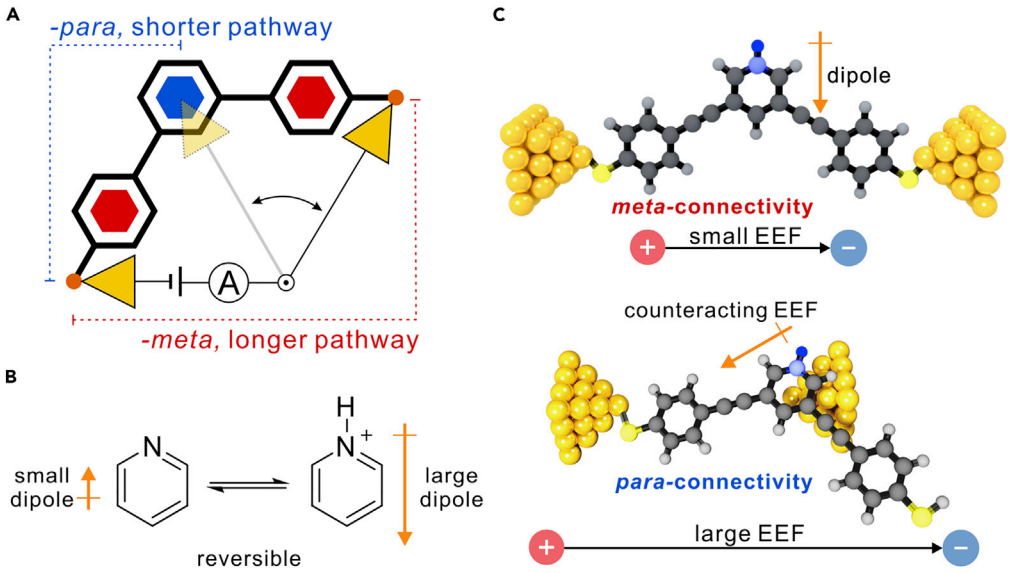

Figure 1. A Single-Molecule Device Based on Connectivity Switching

(A) Schematics of single-molecule switch modulated by connectivity switching. The *meta*-connectivity is associated to a longer transmission pathway with low conductance, whereas the *para*-connectivity is associated to a shorter transmission pathway with high conductance.

(B) The protonation of pyridine leads to a significantly enhanced dipole moment in pyridinium.

(C) Schematics of electric-field-induced connectivity switching between *meta*- and *para*-connectivity. The *para*-connectivity is expected to be favorable when large EEF applied, owing to the counteracting of dipole moments with EEF. See also Figures S11, S25, and S27.

coordination (Aradhya et al., 2012a; Quek et al., 2009), providing a potential anchor to form the in-backbone connectivity (Miguel et al., 2015). Thus, the introduction of EEF into pyridine-based molecular devices provides a promising platform toward the regulating of two possible connectivities in the same molecular skeletons.

In this work, we find that the ring of pyridinium could interact with the gold electrode, so we place pyridine in the middle of the molecular skeletons to set the two possible connectivities: the end-to-end *meta*-connectivity and the in-backbone *para*-connectivity (Figures 1A and 1C). We find that the formation of the two connectivities is controlled by protonation and the applied bias between two electrodes, suggesting that the interaction between dipole moments and the electric field is essential to tune the connectivities of single-molecule junctions. Moreover, the switching between *meta*- and *para*-connectivity is associated with the changing of transport distances from longer to shorter transmission pathways, which enlarge the conductance difference in two connectivities. Utilizing this strategy, we reversibly switch the connectivities in the same molecular skeleton and provide a new concept to efficiently manipulate single-molecule junctions.

RESULTS

Single-Molecule Conductance Measurement

Protonated pyridinium **M1-H** was formed *in-situ* by adding trifluoroacetic acid (TFA) to the solution of **M1** (Figure 2A), which is the neutral state of **M1-H**. The single-molecule conductances are characterized by mechanically controllable break junction (MCBJ) technique (Hong et al., 2012; Li et al., 2017) in the solvent mixture of 1,2,4-trichlorobenzene (TCB)/dichloromethane (DCM). As shown in the inset of Figure 2B, the conductances of single-molecule junctions were recorded during repeated connecting and breaking of two gold electrodes, leading to the individual traces of conductance (on the logarithmic scale) versus stretching distance (Δz). The one-dimensional (1D) conductance histograms of **M1** (blue) and **M1-H** (red) are constructed from ~2000 of such traces. As shown in Figure 2B, the sharp peaks at G_0 represents the formation of gold atomic point contact (Yanson et al., 1998), and the broader peaks are associated to the conductance of corresponding single-molecule junctions, whereas the control experiments in the blank

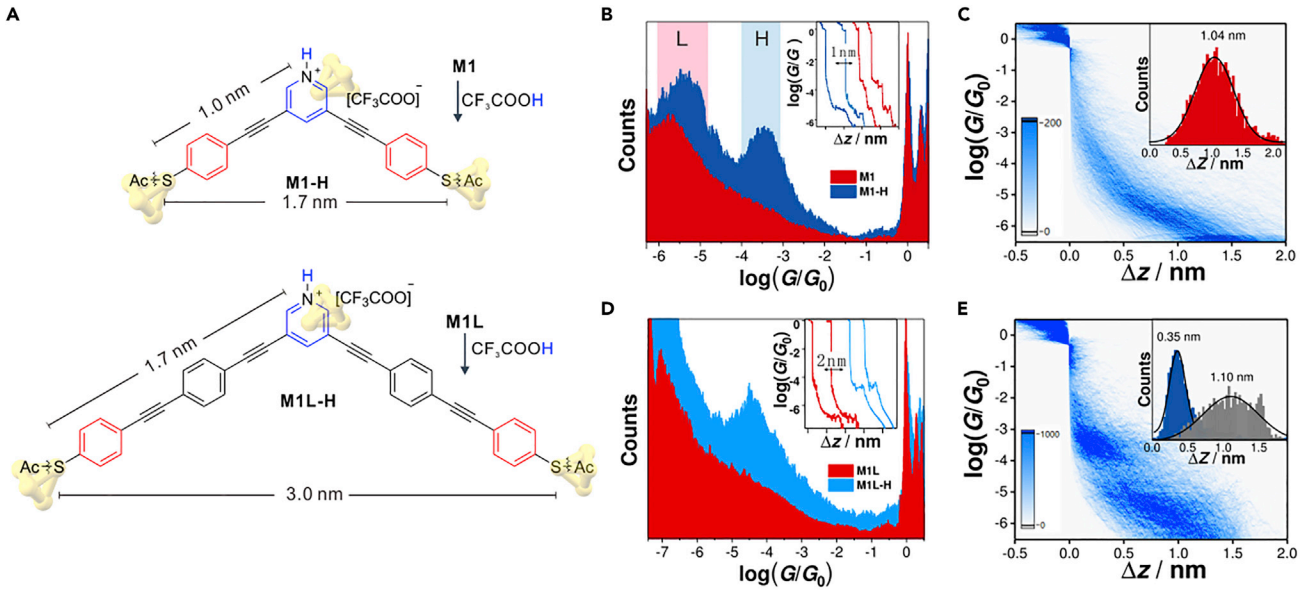

Figure 2. Single-Molecule Conductance Measurement

(A) Molecular structures of **M1-H** and **M1L-H**, which are formed by the protonation of the neutral state **M1** and **M1L** by TFA. The calculated junction lengths for the *meta*- and *para*-connectivity are shown beside.

(B–E) (B) All data-point one-dimensional conductance histograms constructed from 2,000 MCBJ traces of **M1** and **M1-H**. The typical individual traces of **M1** and **M1-H** are shown in the inset. The high- and low-conductance junctions are labeled by "H" and "L" in the blue and red region, respectively. Two-dimensional conductance histograms of **M1** (C) and **M1-H** (E) with stretching distance Δ*z* distributions shown inset. The blue and gray histograms represent the stretching distances of high- and low-conductance junctions of **M1-H**, respectively. (D) All data-point one-dimensional conductance histograms constructed from about 1,000 MCBJ traces of **M1L** and **M1L-H**, respectively. The above measurements were performed in the solvent mixture of TCB/DCM (*v*/*v*, 4/1) at room temperature with 0.10 V bias applied.

See also Figures S1–17, S22, and S23.

solvent did not show such signal (Supplemental Information, Figure S12). We find that **M1** shows a mono conductance peak, with the most probable conductance at $10^{-5.8}$ G_0 (Figure 2B), which is consistent with the previous result with the presence of destructive quantum interference (Liu et al., 2017). Differently, **M1-H** shows two distinct conductance peaks ($10^{-3.5}$ and $10^{-5.4}$ G_0), suggesting the formation of two types of junction geometries, with about two orders of magnitude conductance difference.

The two-dimensional (2D) conductance-displacement histogram of **M1-H** (Figure 2E) demonstrates that the high-conductance junctions have about 0.35 nm stretching distance, which is significantly shorter than the low-conductance junctions of **M1** with a 1.04 nm stretching distance around $10^{-6.0}$ G_0 (Figure 2C). The significantly shorter stretching distance for the high-conductance junction of **M1-H** is associated to the junction geometry formed between one of the –SAc groups and the middle pyridinium ring (Figure 1B), which was confirmed by a series of reference experiments (Supplemental Information, Section 3, Figures S16 and S17). Although pyridine is not a good candidate to form the in-backbone connectivity (Liu et al., 2017; Miguel et al., 2015), the *in-situ* formed pyridinium is feasible to form the in-backbone connectivity. We think such feasibility is associated with the significantly enhanced dipole moments in pyridiniums (Figure S25A), which would have a stronger interaction with the electric field applied by the two electrodes, playing an essential role in favoring the formation of the high-conductance junctions in **M1-H**. Meanwhile, the features of single-molecule conductance between **M1** and **M1-H** could be reversibly emerged when acid or base added (Figure S20).

The strategy to tune the connectivity of single-molecule junctions offers the chance to further enhance the conductance difference between the low- and high-conductance junctions, by enlarging the difference of charge transport distances in between (Cheng et al., 2011; Choi et al., 2008; Dell et al., 2015). Toward this goal, we designed molecules **M1L-H** formed by the protonation of **M1L**, leading to a 1.3 nm difference between two possible connectivities (Figure 2A), which is almost two-fold than that in **M1-H** (Figure S23). As shown in Figure 2D, **M1L** shows a mono conductance peak at $10^{-7.1}$ G_0, attributing to the end-to-end

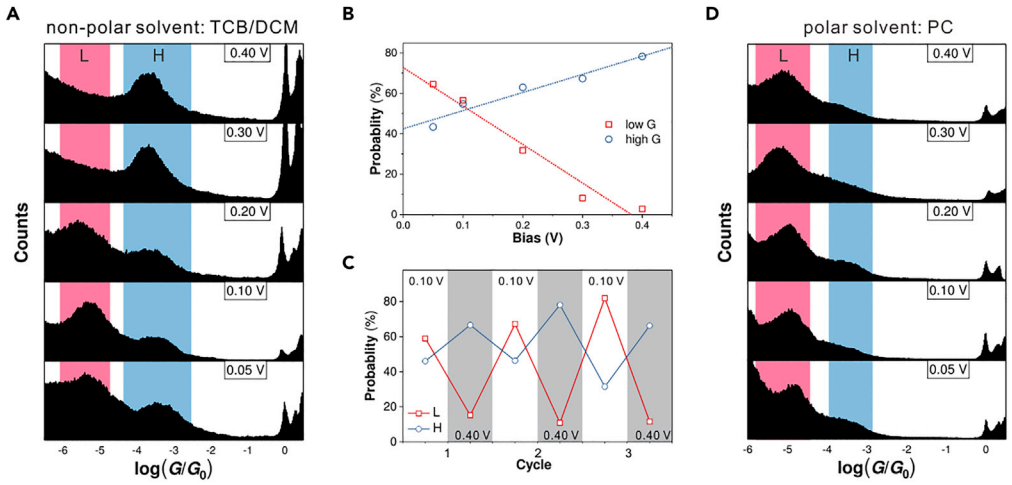

Figure 3. Bias-Dependent Junction Formation Probability

(A) One-dimensional conductance histograms of **M1-H** with a different bias applied, in the solvent TCB/DCM mixture (*v*/*v*, 4/1).

(B) The junction formation probability of **M1-H** for the corresponding low- and high-conductance junctions, respectively are labeled by the blue and red dashed lines plotted by the linear fitting.

(C) The junction formation probability for the low- and high-conductance junctions of **M1-H** with 0.10 and 0.40 V bias applied alternately.

(D) One-dimensional conductance histograms of **M1-H** with a different bias applied, in the solvent of propylene carbonate (PC). The above measurements were performed at room temperature.

See also Figures S17–S19, S21, S24, and S26.

meta-connectivity (Figure S22). The conductance peak for the protonated **M1L-H** locates at $10^{-4.5}$ G_0, attributing to the high-conductance junctions, whereas the low-conductance junctions of **M1L-H** have the conductance below detecting limit, suggesting that the conductance difference between the two connectivities in **M1L-H** is increasing to ~400 times. The results suggest that the manipulation of the difference of charge transport distances would lead to larger conductance difference in the two connectivities. More importantly, the conductance difference can be fine-tuned and further increased by this strategy, but the quantitative investigation of a molecular system with even more substantial conductance difference is restricted by the detecting limit of single-molecule conductance measurement.

Revealing the Role of the Electric Field

To understand the interaction between the molecular component and the electric field, we varied the bias voltages applied to the molecular junctions in the single-molecule conductance measurement. On account of the detecting limit, we focused the investigation on **M1-H**. Firstly, by increasing the bias from 0.05 to 0.40 V for the MCBJ measurement of **M1-H** in a nonpolar solvent (TCB/DCM), as shown in Figure 3A, we find that the formation of low-conductance junctions in **M1-H** is gradually suppressed and almost completely suppressed in the bias of 0.40 V. Meanwhile, the formation of high-conductance junctions in **M1-H** becomes more and more favorable with the increasing of bias. We quantitatively characterize the junction formation probability for both the low- and high-conductance junctions of **M1-H** in different bias (Figure S18); as shown in Figure 3B, we find that the low-conductance junctions are dominant in 0.05 V bias, whereas the high-conductance junctions become dominant when the bias is higher than 0.20 V. From the overall trend, the junction formation probability for the high-conductance junctions of **M1-H** has a positive correlation to the bias, which has a negative correlation to the low-conductance junctions of **M1-H**. Moreover, when the bias is switched between 0.10 and 0.40 V, as shown in Figure 3C, we find the high- and low-conductance junctions of **M1-H** become dominated alternately in a reversible way (Figure S19).

To further reveal the role of the electric field, we use a polar solvent, propylene carbonate (PC), to characterize the single-molecule conductance of **M1-H**. As shown in Figure 3D, the high-conductance junctions of **M1-H** are significantly suppressed even in higher bias. We also find that such bias-dependent junction

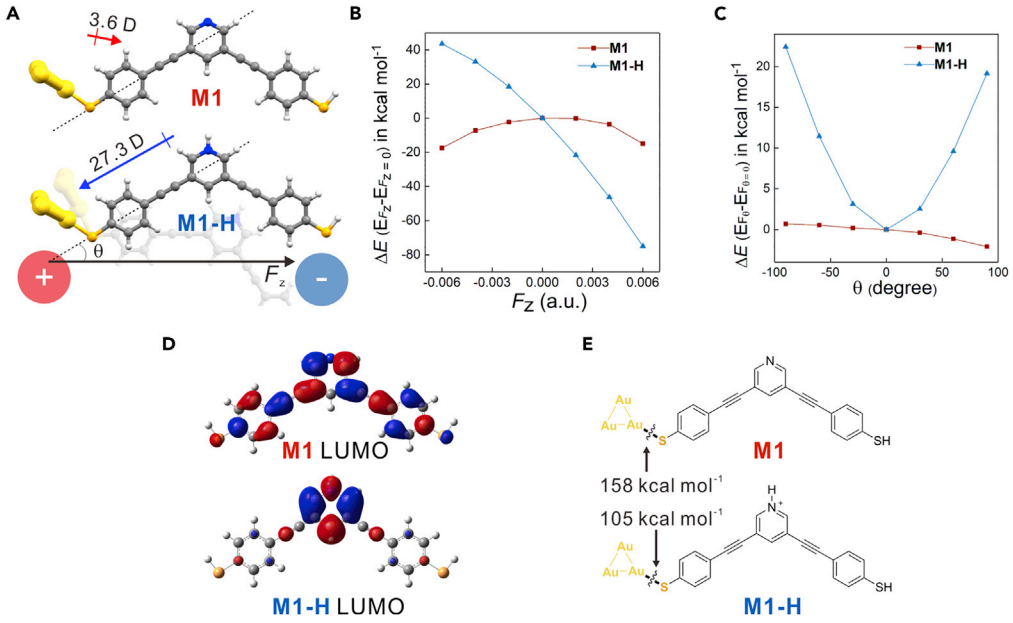

Figure 4. Theoretical Calculation

(A) The strength and direction of dipole moments for **M1** and **M1-H** were shown by the red and blue arrows nearby; the angle between molecule orientation (dash line) and applied electric field F_z was defined as θ. Symbol D represents Debye, the unit of dipole moments.

(B) Plots of total energy difference ΔE (E_{Fz} - $E_{Fz\,=\,0}$) versus the applied electric field when θ = 0.

(C) Plots of total energy difference ΔE (E_θ - $E_{\theta\,=\,0}$) versus θ, with electric field F_z = + 0.002 a.u. applied.

(D) The orbital isosurfaces of LUMOs of **M1** and the cation of **M1-H**.

(E) The Au-S covalent bonds formation energy of **M1** and **M1-H**.

See also Figures S21 and S24.

formation probability of **M1-H** observed in nonpolar solvent also vanished in the polar solvent. In consideration of the changing of the equilibrium between **M1** and **M1-H** when we use PC, a polar solvent showing weak basicity, we also characterized the response of the methylated pyridinium of **M1** to electric field (Figure S17). We also find that the bias-dependent suppression of the low conductance junctions in non-polar solvent (Figure S17D) also vanish in polar solvent (Figure S17E), suggesting the importance of the dielectric constant in tuning such electric-field-induced connectivity switching. Because the polar solvent results in the attenuation of the electric field (Bermudez et al., 2000), the absence of high-conductance junctions in **M1-H** suggests the importance of the electric field to regulate the connectivities of single-molecule junctions.

Theoretical Calculations

To investigate the connectivity switching mechanism in **M1-H**, we carried density functional theory (DFT) calculation to study the different binding geometries between **M1** and **M1-H**. We find that the dipole moment of **M1-H** is eight times larger than **M1** (Figure 4A), attributing to the net positive charge in **M1-H** (Figure S25). The models with one of the sulfur binding to the gold electrode are used for analyzing. The effect of EEF was evaluated by the total energy changing versus the strength of EEF and the relative orientation between EEF and molecules (Figure 4A dash line). As shown in Figure 4B, fixing the EEF paralleled to the dashed line (θ = 0), with the strength of EEF changing from −0.006 to 0.006 a.u. (−3.1 to 3.1 V/nm), the total energy of **M1-H** varies about 120 kcal mol^{-1}, whereas such an effect for **M1** is negligible. Upon changing θ from −90° to 90° with fixed EEF strength (+0.002 a.u.), as shown in Figure 4C, the most favorable molecular orientation for **M1-H** is the in-backbone connectivity (θ = 0) with a parallel orientation to EEF, whereas **M1** does not show explicit dependency to θ. The calculation result is consistent with the bias-dependent junction formation probability, in which the in-backbone connectivity of **M1-H** becomes more and more dominant in higher bias (Figure 3A). Besides the difference of dipole moments between **M1** and **M1-H**, the electrostatic potential distributions of **M1-H** shows significantly high positive charge distribution around the pyridinium ring (Figure S25B), so that the electrostatic attraction between

the electrode and the pyridinium ring of **M1-H** would be another factor in facilitating the formation of high-conductance junctions in **M1-H**.

We also find that the formation of pyridinium has a distinct effect on their frontier orbitals. As shown in Figure 4D, the LUMO of **M1-H** is localized at the pyridinium ring, which is distinct to **M1** with its LUMO delocalized around the molecular skeleton. The localized LUMO of **M1-H** weakens the back-donating bonding from gold to sulfur, leading to weaker Au-S bond, which is confirmed by DFT calculation (Figure 4E) and surface-enhanced Raman spectra that the vibration mode of Au-S was red-shifted from 249 cm^{-1} in **M1** to 234 cm^{-1} in **M1-H** (Figure S21) (Kocharova et al., 2007). The weaker Au-S bond in **M1-H** reduces the competition to form the end-to-end connectivity between two sulfurs and makes the formation of the in-backbone connectivity more favorable. Thus, we think both the electric field and the weakened Au-S bonds contribute to the formation of high-conductance junctions in **M1-H**.

DISCUSSION

In conclusion, we have developed an electric-field-induced strategy for reversible switching the connectivities of single-molecule junctions. Through the switching from longer *meta*-connectivity to shorter *para*-connectivity, we manipulate the charge-transport distances, which significantly enhance the conductance difference between two connectivities. The mechanism of the switching is further investigated by experiments and DFT calculation, revealing that the protonation-enhanced dipole moments have significant interaction with the electric field, which favors the formation of in-backbone *para*-connectivity. Our studies suggest that the interplay between the dipole moment of molecules and EEF will lead to a reversible connectivity switching strategy, which would provide a new concept to manipulate the molecule-electrode interaction and be promising for constructing new conceptual molecular devices.

Limitations of the Study

The switching from the end-to-end connection to the in-backbone connection of **M1-H** may also lead to the switching of quantum interference in the charge transport through the single-molecule junctions. For instance, the changes from *meta*-connection to *para*-connection may switch the patterns of quantum interference from destructive to constructive states and also offer a new opportunity for interference-based molecular devices. However, the understanding of quantum interference patterns needs further investigations, which are challenging to be accomplished at the current stage.

METHODS

All methods can be found in the accompanying Transparent Methods supplemental file.

SUPPLEMENTAL INFORMATION

Supplemental Information can be found online at https://doi.org/10.1016/j.isci.2019.100770.

ACKNOWLEDGMENTS

This work was supported by the National Key R&D Program of China (2017YFA0204902), the National Natural Science Foundation of China (Nos, 21673195, 21722305, 21703188, U1705254), China Postdoctoral Science Foundation (No. 2017M622060), and the Fundamental Research Funds for Xiamen University (20720190002).

AUTHOR CONTRIBUTIONS

W. H. and H. X. originally conceived the concept and designed the experiments. W.H., H.X., C.T., J.L., Z.C, J.Z., Z.C., and J.S. prepared the manuscript using feedback from other authors. C.T., Y.Y., and X.H. carried out the single-molecule conductance measurements. Synthetic work and Raman spectroscopic studies were carried out by C.T., J.Z., J.B., and Z.Y.; calculations were carried out by C.T. and L.C. All authors have approved the final version of the manuscript.

DECLARATION OF INTERESTS

The authors declare no competing interests.

Received: November 7, 2018
Revised: November 13, 2019
Accepted: December 9, 2019
Published: January 24, 2020

REFERENCES

Agraït, N., Yeyati, A.L., and van Ruitenbeek, J.M. (2003). Quantum properties of atomic-sized conductors. Phys. Rep. *377*, 81–279.

Aradhya, S.V., Frei, M., Hybertsen, M.S., and Venkataraman, L. (2012a). Van der waals interactions at metal/organic interfaces at the single-molecule level. Nat. Mater. *11*, 872–876.

Aradhya, S.V., Meisner, J.S., Krikorian, M., Ahn, S., Parameswaran, R., Steigerwald, M.L., Nuckolls, C., and Venkataraman, L. (2012b). Dissecting contact mechanics from quantum interference in single-molecule junctions of stilbene derivatives. Nano Lett. *12*, 1643–1647.

Aragonès, A.C., Haworth, N.L., Darwish, N., Ciampi, S., Bloomfield, N.J., Wallace, G.G., Diez-Perez, I., and Coote, M.L. (2016). Electrostatic catalysis of a diels–alder reaction. Nature *531*, 88–91.

Arroyo, C.R., Tarkuc, S., Frisenda, R., Seldenthuis, J.S., Woerde, C.H.M., Eelkema, R., Grozema, F.C., and van der Zant, H.S.J. (2013). Signatures of quantum interference effects on charge transport through a single benzene ring. Angew. Chem. Int. Ed. *52*, 3152–3155.

Bai, J., Daaoub, A., Sangtarash, S., Li, X., Tang, Y., Zou, Q., Sadeghi, H., Liu, S., Huang, X., Tan, Z., et al. (2019). Anti-resonance features of destructive quantum interference in single-molecule thiophene junctions achieved by electrochemical gating. Nat. Mater. *18*, 364–369.

Ballmann, S., Härtle, R., Coto, P.B., Elbing, M., Mayor, M., Bryce, M.R., Thoss, M., and Weber, H.B. (2012). Experimental evidence for quantum interference and vibrationally induced decoherence in single-molecule junctions. Phys. Rev. Lett. *109*, 056801.

Bermudez, V., Capron, N., Gase, T., Gatti, F.G., Kajzar, F., Leigh, D.A., Zerbetto, F., and Zhang, S. (2000). Influencing intramolecular motion with an alternating electric field. Nature *406*, 608–611.

Bi, H., Palma, C.A., Gong, Y., Hasch, P., Elbing, M., Mayor, M., Reichert, J., and Barth, J.V. (2018). Voltage-driven conformational switching with distinct Raman signature in a single-molecule junction. J. Am. Chem. Soc. *140*, 4835–4840.

Brooke, R.J., Szumski, D.S., Vezzoli, A., Higgins, S.J., Nichols, R.J., and Schwarzacher, W. (2018). Dual control of molecular conductance through ph and potential in single-molecule devices. Nano Lett. *18*, 1317–1322.

Carlotti, M., Soni, S., Kumar, S., Ai, Y., Sauter, E., Zharnikov, M., and Chiechi, R.C. (2018). Two-terminal molecular memory through reversible switching of quantum interference features in tunneling junctions. Angew. Chem. Int. Ed. *57*, 15681–15685.

Chen, X., Roemer, M., Yuan, L., Du, W., Thompson, D., del Barco, E., and Nijhuis, C.A. (2017). Molecular diodes with rectification ratios exceeding 105 driven by electrostatic interactions. Nat. Nanotechnol. *12*, 797.

Cheng, Z.L., Skouta, R., Vazquez, H., Widawsky, J.R., Schneebeli, S., Chen, W., Hybertsen, M.S., Breslow, R., and Venkataraman, L. (2011). In situ formation of highly conducting covalent au-c contacts for single-molecule junctions. Nat. Nanotechnol. *6*, 353–357.

Choi, S.H., Kim, B., and Frisbie, C.D. (2008). Electrical resistance of long conjugated molecular wires. Science *320*, 1482–1486.

Ciampi, S., Darwish, N., Aitken, H.M., Diez-Perez, I., and Coote, M.L. (2018). Harnessing electrostatic catalysis in single molecule, electrochemical and chemical systems: a rapidly growing experimental tool box. Chem. Soc. Rev. *47*, 5146–5164.

Darwish, N., Diez-Perez, I., Da Silva, P., Tao, N.J., Gooding, J.J., and Paddon-Row, M.N. (2012). Observation of electrochemically controlled quantum interference in a single anthraquinone-based norbornylogous bridge molecule. Angew. Chem. Int. Ed. *51*, 3203–3206.

Dell, E.J., Capozzi, B., Xia, J., Venkataraman, L., and Campos, L.M. (2015). Molecular length dictates the nature of charge carriers in single-molecule junctions of oxidized oligothiophenes. Nat. Chem. *7*, 209–214.

Frisenda, R., Janssen, V.A., Grozema, F.C., van der Zant, H.S., and Renaud, N. (2016). Mechanically controlled quantum interference in individual pi-stacked dimers. Nat. Chem. *8*, 1099–1104.

Fujii, S., Tada, T., Komoto, Y., Osuga, T., Murase, T., Fujita, M., and Kiguchi, M. (2015). Rectifying electron-transport properties through stacks of aromatic molecules inserted into a self-assembled cage. J. Am. Chem. Soc. *137*, 5939–5947.

Garner, M.H., Li, H., Chen, Y., Su, T.A., Shangguan, Z., Paley, D.W., Liu, T., Ng, F., Li, H., Xiao, S., et al. (2018). Comprehensive suppression of single-molecule conductance using destructive σ-interference. Nature *558*, 415–419.

Gerhard, L., Edelmann, K., Homberg, J., Valášek, M., Bahoosh, S.G., Lukas, M., Pauly, F., Mayor, M., and Wulfhekel, W. (2017). An electrically actuated molecular toggle switch. Nat. Commun. *8*, 14672.

Guedon, C.M., Valkenier, H., Markussen, T., Thygesen, K.S., Hummelen, J.C., and Van Der Molen, S.J. (2012). Observation of quantum interference in molecular charge transport. Nat. Nanotechnol. *7*, 305–309.

Hines, T., Díez-Pérez, I., Nakamura, H., Shimazaki, T., Asai, Y., and Tao, N. (2013). Controlling formation of single-molecule junctions by electrochemical reduction of diazonium terminal groups. J. Am. Chem. Soc. *135*, 3319–3322.

Hong, W., Manrique, D.Z., Moreno-Garcia, P., Gulcur, M., Mishchenko, A., Lambert, C.J., Bryce, M.R., and Wandlowski, T. (2012). Single molecular conductance of tolanes: experimental and theoretical study on the junction evolution dependent on the anchoring group. J. Am. Chem. Soc. *134*, 2292–2304.

Huang, X., Tang, C., Li, J., Chen, L.C., Zheng, J., Zhang, P., Le, J., Li, R., Li, X., Liu, J., et al. (2019). Electric field-induced selective catalysis of single-molecule reaction. Sci. Adv. *5*, eaaw3072.

Kocharova, N., Ääritalo, T., Leiro, J., Kankare, J., and Lukkari, J. (2007). Aqueous dispersion, surface thiolation, and direct self-assembly of carbon nanotubes on gold. Langmuir *23*, 3363–3371.

Koren, E., Leven, I., Lortscher, E., Knoll, A., Hod, O., and Duerig, U. (2016). Coherent commensurate electronic states at the interface between misoriented graphene layers. Nat. Nanotechnol. *11*, 752–757.

Lambert, C.J. (2015). Basic concepts of quantum interference and electron transport in single-molecule electronics. Chem. Soc. Rev. *44*, 875–888.

Leary, E., La Rosa, A., González, M.T., Rubio-Bollinger, G., Agraït, N., and Martín, N. (2015). Incorporating single molecules into electrical circuits. The role of the chemical anchoring group. Chem. Soc. Rev. *44*, 920–942.

Li, L.W., Lo, W.Y., Cai, Z.X., Zhang, N., and Yu, L.P. (2016). Proton-triggered switch based on a molecular transistor with edge-on gate. Chem. Sci. *7*, 3137–3141.

Li, R., Lu, Z., Cai, Y., Jiang, F., Tang, C., Chen, Z., Zheng, J., Pi, J., Zhang, R., Liu, J., et al. (2017). Switching of charge transport pathways via delocalization changes in single-molecule metallacycles junctions. J. Am. Chem. Soc. *139*, 14344–14347.

Li, Y., Buerkle, M., Li, G., Rostamian, A., Wang, H., Wang, Z., Bowler, D.R., Miyazaki, T., Xiang, L., Asai, Y., et al. (2019). Gate controlling of quantum interference and direct observation of anti-resonances in single molecule charge transport. Nat. Mater. *18*, 357–363.

Liu, X., Sangtarash, S., Reber, D., Zhang, D., Sadeghi, H., Shi, J., Xiao, Z.Y., Hong, W., Lambert, C.J., and Liu, S.X. (2017). Gating of quantum interference in molecular junctions by heteroatom substitution. Angew. Chem. Int. Ed. *56*, 173–176.

Liu, J., Huang, X., Wang, F., and Hong, W. (2019). Quantum interference effects in charge transport through single-molecule junctions: detection,

manipulation, and application. Acc. Chem. Res. *52*, 151–160.

Lörtscher, E., Ciszek, J.W., Tour, J., and Riel, H.J.S. (2006). Reversible and controllable switching of a single-molecule junction. Small *2*, 973–977.

Mayor, M., Weber, H.B., Reichert, J., Elbing, M., von Hänisch, C., Beckmann, D., and Fischer, M. (2003). Electric current through a molecular rod—relevance of the position of the anchor groups. Angew. Chem. Int. Ed. *42*, 5834–5838.

Meded, V., Bagrets, A., Arnold, A., and Evers, F.J.S. (2009). Molecular switch controlled by pulsed bias voltages. Small *5*, 2218–2223.

Meisner, J.S., Ahn, S., Aradhya, S.V., Krikorian, M., Parameswaran, R., Steigerwald, M., Venkataraman, L., and Nuckolls, C. (2012). Importance of direct metal-pi coupling in electronic transport through conjugated single-molecule junctions. J. Am. Chem. Soc. *134*, 20440–20445.

Meng, L., Xin, N., Hu, C., Wang, J., Gui, B., Shi, J., Wang, C., Shen, C., Zhang, G., Guo, H., et al. (2019). Side-group chemical gating via reversible optical and electric control in a single molecule transistor. Nat. Commun. *10*, 1450.

Miguel, D., Alvarez de Cienfuegos, L., Martín-Lasanta, A., Morcillo, S.P., Zotti, L.A., Leary, E., Bürkle, M., Asai, Y., Jurado, R., and Cardenas, D.J. (2015). Toward multiple conductance pathways with heterocycle-based oligo (phenyleneethynylene) derivatives. J. Am. Chem. Soc. *137*, 13818–13826.

Moth-Poulsen, K., and Bjørnholm, T. (2009). Molecular electronics with single molecules in solid-state devices. Nat. Nanotechnol. *4*, 551–556.

Olavarria-Contreras, I.J., Etcheverry-Berrios, A., Qian, W.J., Gutierrez-Ceron, C., Campos-Olguin, A., Sanudo, E.C., Dulic, D., Ruiz, E., Aliaga-Alcalde, N., Soler, M., et al. (2018). Electric-field induced bistability in single-molecule conductance measurements for boron coordinated curcuminoid compounds. Chem. Sci. *9*, 6988–6996.

Quek, S.Y., Kamenetska, M., Steigerwald, M.L., Choi, H.J., Louie, S.G., Hybertsen, M.S., Neaton, J.B., and Venkataraman, L. (2009). Mechanically controlled binary conductance switching of a single-molecule junction. Nat. Nanotechnol. *4*, 230–234.

Ratner, M. (2013). A brief history of molecular electronics. Nat. Nanotechnol. *8*, 378–381.

Shaik, S., Mandal, D., and Ramanan, R. (2016). Oriented electric fields as future smart reagents in chemistry. Nat. Chem. *8*, 1091–1098.

Shaik, S., Ramanan, R., Danovich, D., and Mandal, D. (2018). Structure and reactivity/selectivity control by oriented-external electric fields. Chem. Soc. Rev. *47*, 5125–5145.

Solomon, G.C., Herrmann, C., Hansen, T., Mujica, V., and Ratner, M.A. (2010). Exploring local currents in molecular junctions. Nat. Chem. *2*, 223–228.

Su, T.A., Neupane, M., Steigerwald, M.L., Venkataraman, L., and Nuckolls, C. (2016). Chemical principles of single-molecule electronics. Nat. Rev. Mater. *1*, 16002.

Tang, C., Chen, L., Zhang, L., Chen, Z., Li, G., Yan, Z., Lin, L., Liu, J., Huang, L., Ye, Y., et al. (2019). Multicenter-bond-based quantum interference in charge transport through single-molecule carborane junctions. Angew. Chem. Int. Ed. *58*, 10601–10605.

Thompson, D., and Nijhuis, C.A. (2016). Even the odd numbers help: failure modes of sam-based tunnel junctions probed via odd-even effects revealed in synchrotrons and supercomputers. Acc. Chem. Res. *49*, 2061–2069.

Vergeer, F.W., Chen, X.D., Lafolet, F., De Cola, L., Fuchs, H., and Chi, L.F. (2006). Ultrathin luminescent films of rigid dinuclear ruthenium(ii) trisbipyridine complexes. Adv. Funct. Mater. *16*, 625–632.

Wang, Z., Danovich, D., Ramanan, R., and Shaik, S. (2018). Oriented-external electric fields create absolute enantioselectivity in diels–alder reactions: importance of the molecular dipole moment. J. Am. Chem. Soc. *140*, 13350–13359.

Xiang, D., Wang, X., Jia, C., Lee, T., and Guo, X. (2016a). Molecular-scale electronics: from concept to function. Chem. Rev. *116*, 4318–4440.

Xiang, L.M., Hines, T., Palma, J.L., Lu, X.F., Mujica, V., Ratner, M.A., Zhou, G., and Tao, N.J. (2016b). Non-exponential length dependence of conductance in iodide terminated oligothiophene single-molecule tunneling junctions. J. Am. Chem. Soc. *138*, 679–687.

Yanson, A.I., Bollinger, G.R., van den Brom, H.E., Agrait, N., and van Ruitenbeek, J.M. (1998). Formation and manipulation of a metallic wire of single gold atoms. Nature *395*, 783–785.

Yoshizawa, K., Tada, T., and Staykov, A. (2008). Orbital views of the electron transport in molecular devices. J. Am. Chem. Soc. *130*, 9406–9413.

Zhang, L., Laborda, E., Darwish, N., Noble, B.B., Tyrell, J.H., Pluczyk, S., Le Brun, A.P., Wallace, G.G., Gonzalez, J., and Coote, M.L. (2018). Electrochemical and electrostatic cleavage of alkoxyamines. J. Am. Chem. Soc. *140*, 766–774.

iScience, Volume *23*

Supplemental Information

Electric-Field-Induced Connectivity Switching in Single-Molecule Junctions

Chun Tang, Jueting Zheng, Yiling Ye, Junyang Liu, Lijue Chen, Zhewei Yan, Zhixin Chen, Lichuan Chen, Xiaoyan Huang, Jie Bai, Zhaobin Chen, Jia Shi, Haiping Xia, and Wenjing Hong

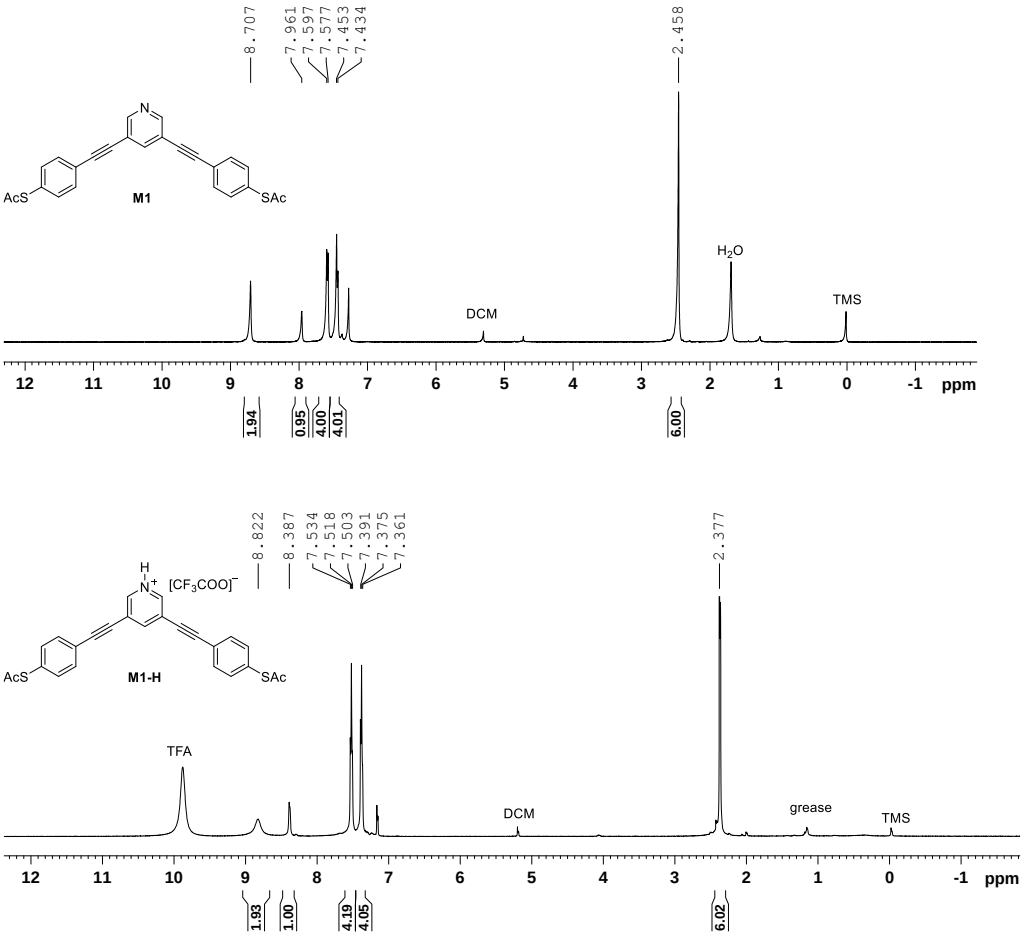

Figure S1. ^{1}H NMR ($CDCl_3$, 500 MHz) spectrum of compound **M1-H** in comparison with **M1**. Related to Figure 2.

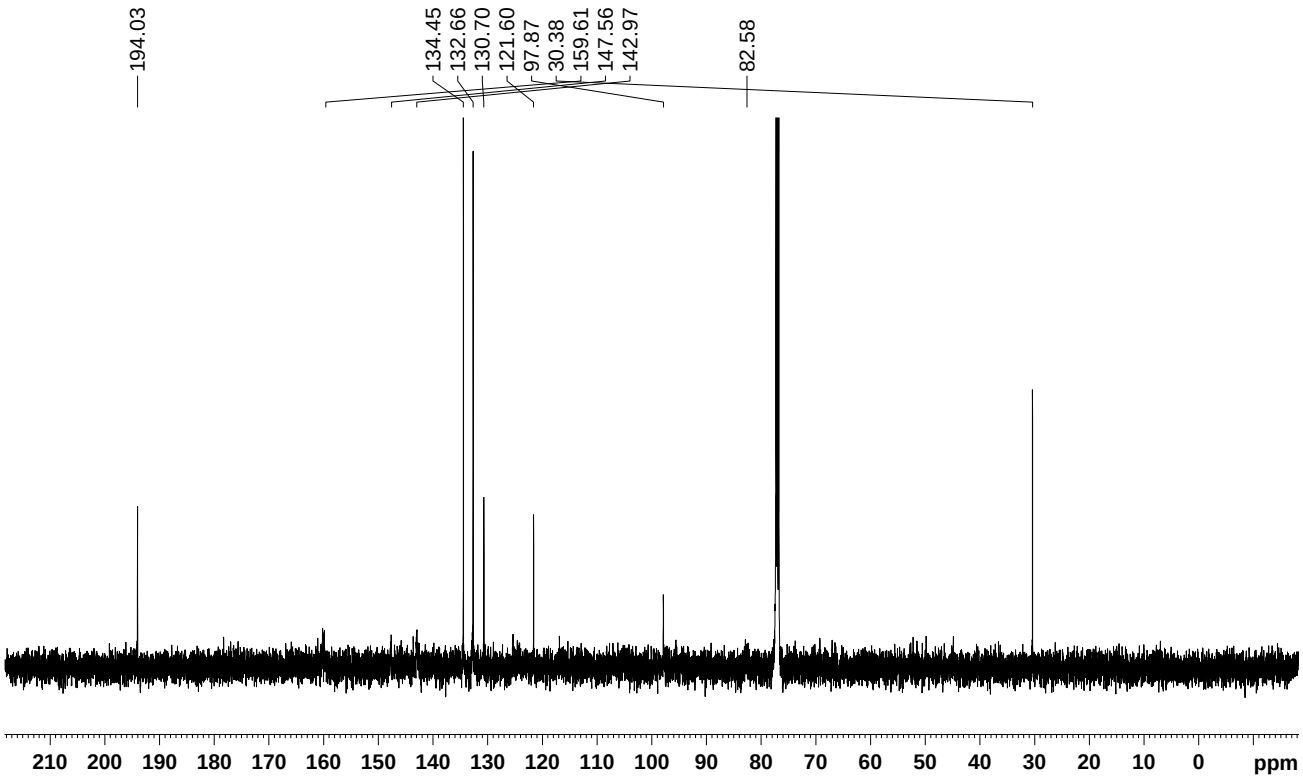

Figure S2. ^{13}C NMR ($CDCl_3$, 125 MHz) spectrum of compound **M1-H**. Related to Figure 2.

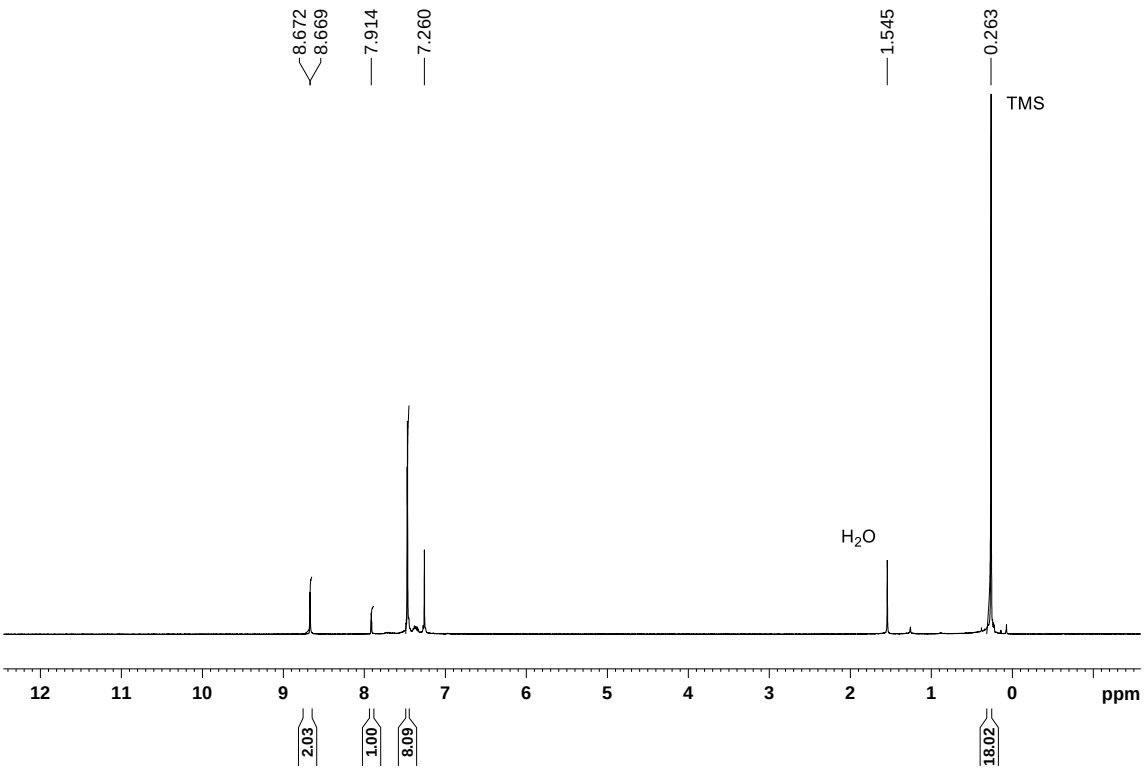

Figure S3. ^{1}H NMR ($CDCl_3$, 500 MHz) spectrum of compound **2**. Related to Figure 2.

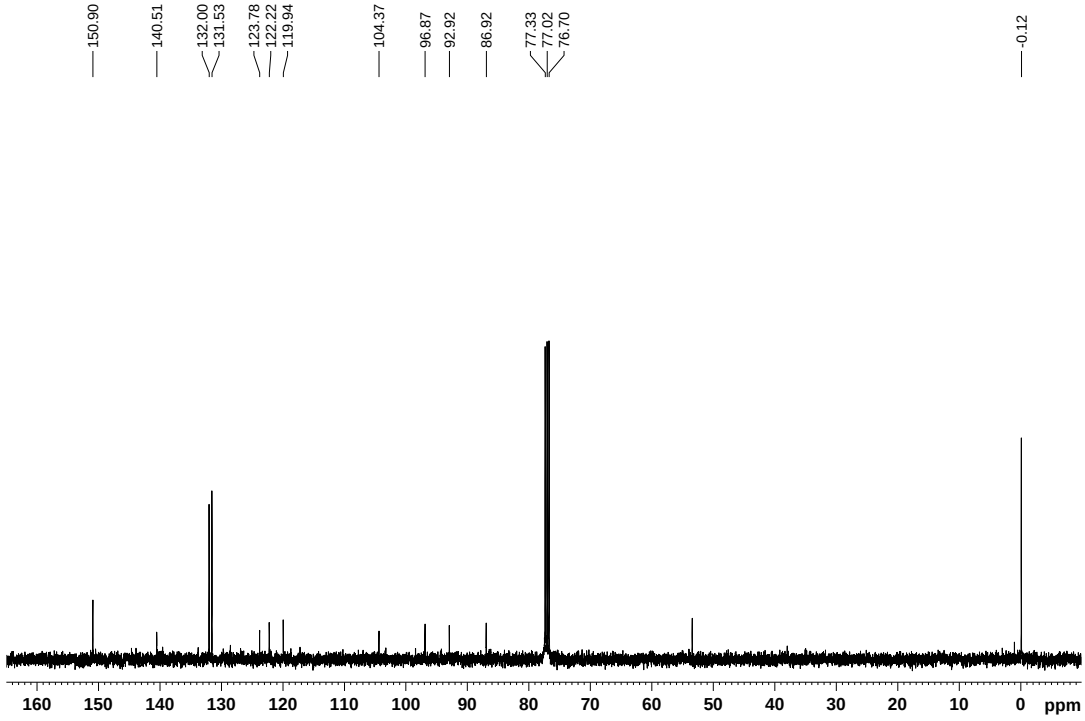

Figure S4. ^{13}C NMR ($CDCl_3$, 125 MHz) spectrum of compound **2**. Related to Figure 2.

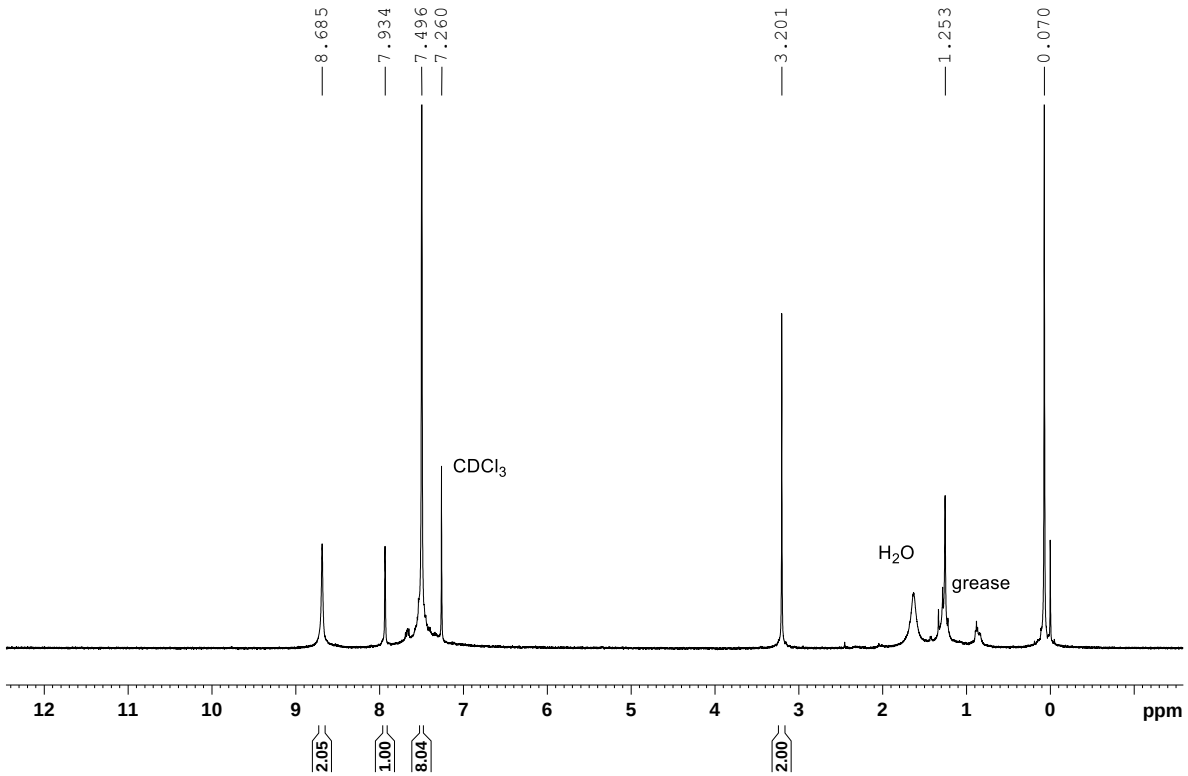

Figure S5. ^{1}H NMR ($CDCl_3$, 500 MHz) spectrum of compound **3**. Related to Figure 2.

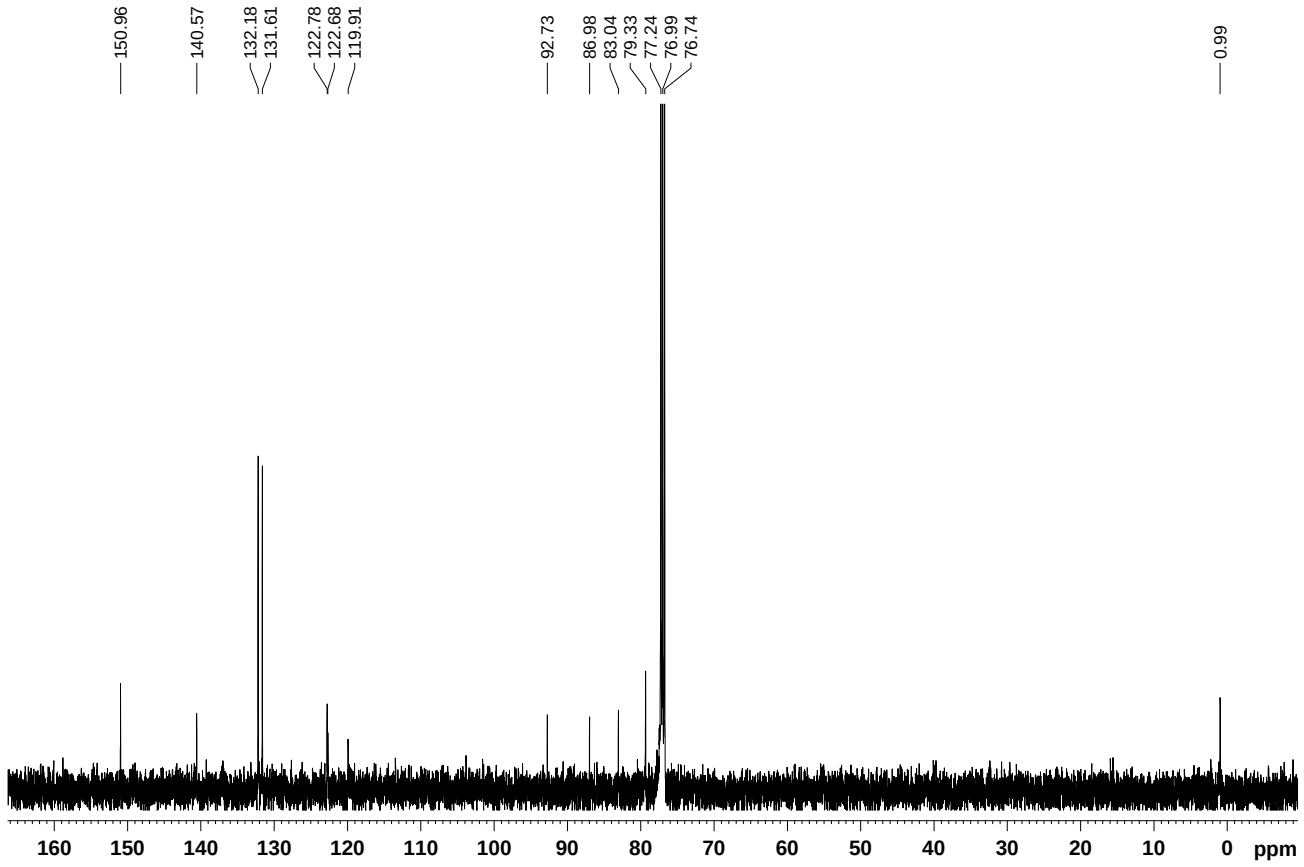

Figure S6. ^{13}C NMR ($CDCl_3$, 125 MHz) spectrum of compound **3**. Related to Figure 2.

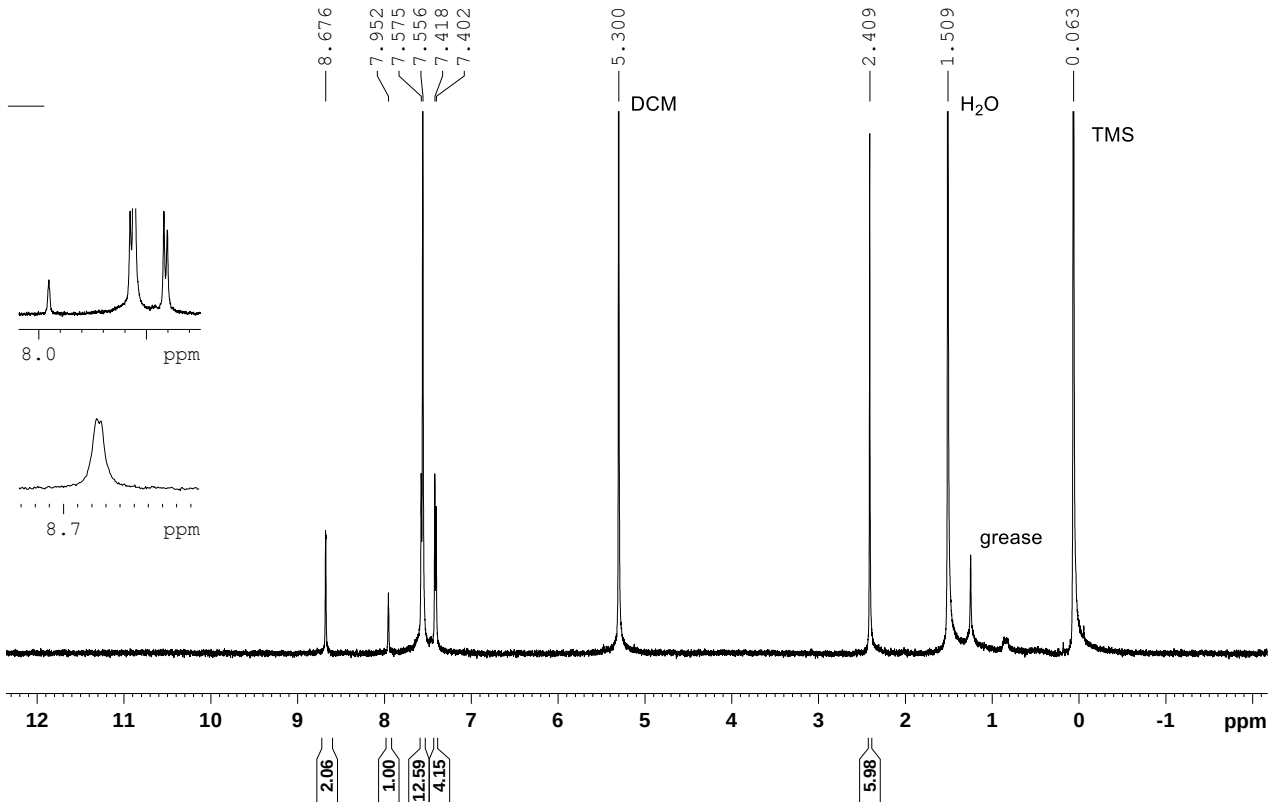

Figure S7. ^{1}H NMR (CD_2Cl_2, 500 MHz) spectrum of compound **M1L**. Related to Figure 2.

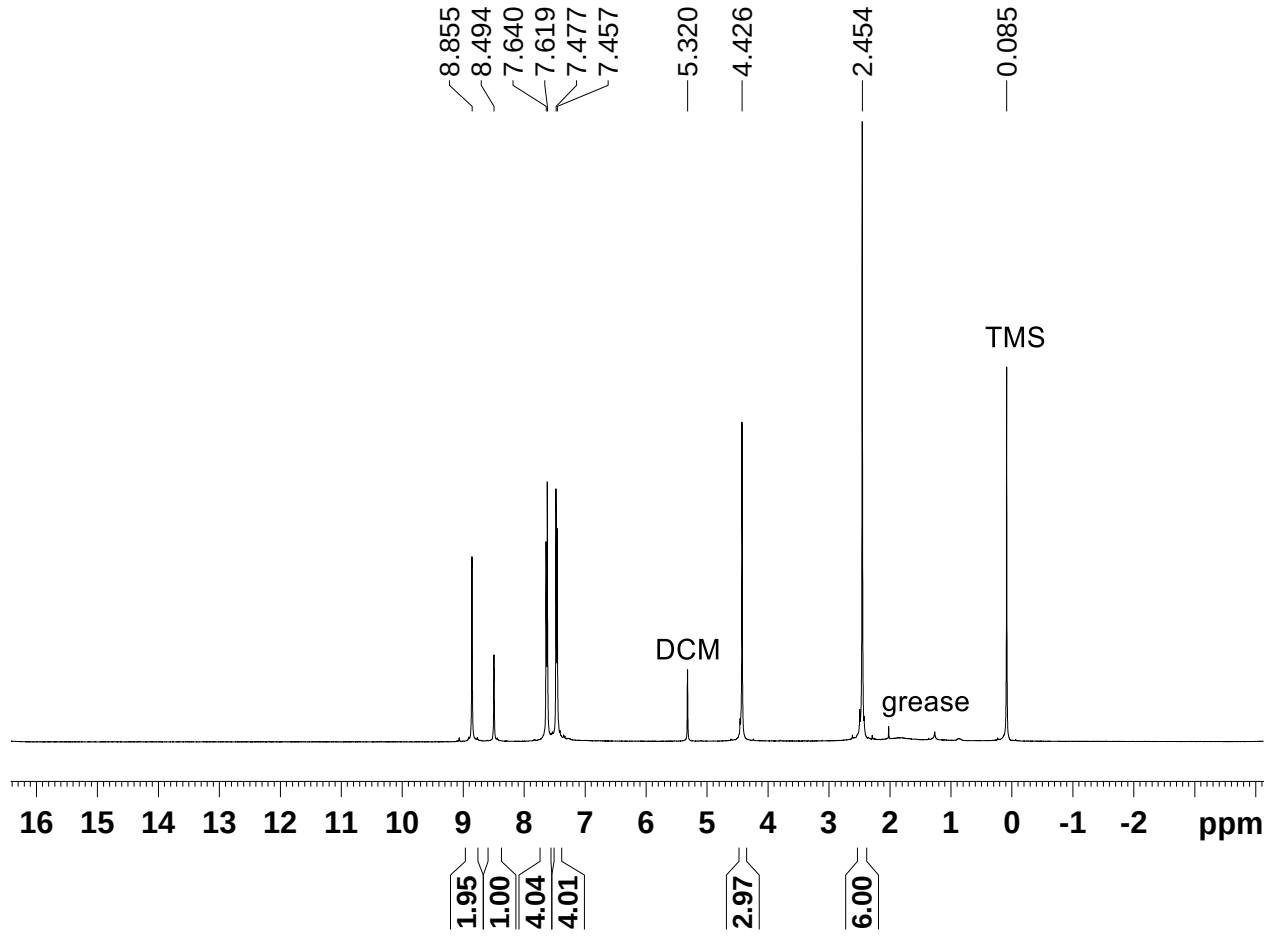

Figure S8. ^{1}H NMR (CD_2Cl_2, 500 MHz) spectrum of compound **M1-Me**. Related to Figure 2.

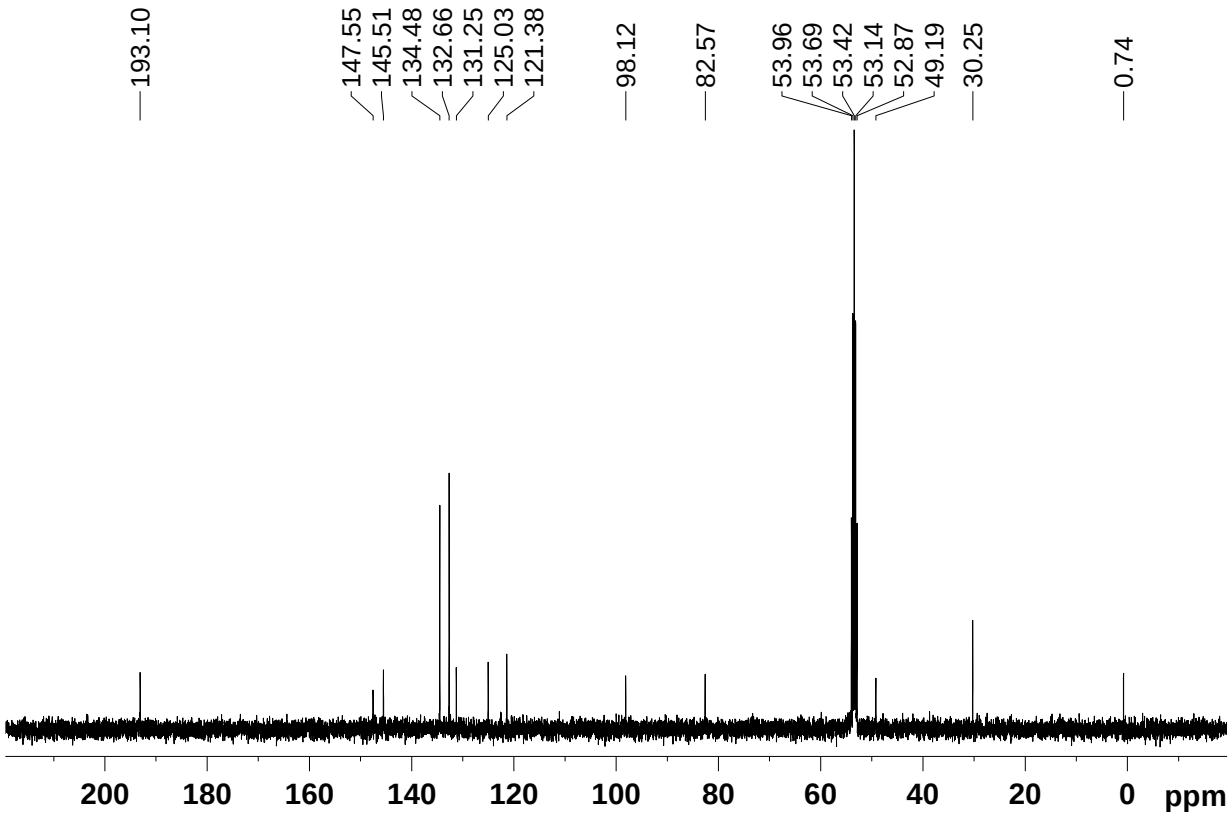

Figure S9. ^{13}C NMR (CD_2Cl_2, 125 MHz) spectrum of compound **M1-Me**. Related to Figure 2.

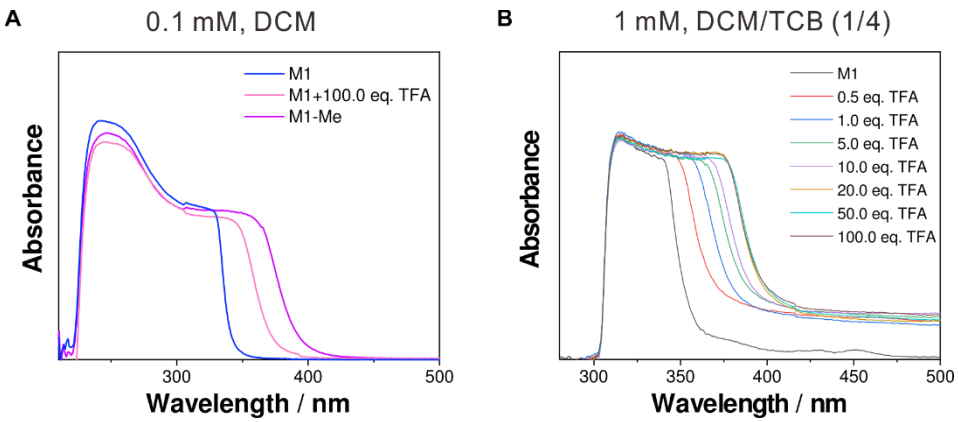

Figure S10. (**A**) UV-Vis spectra of methylated pyridiniums **M1-H** and **M1-Me** and their pyridine parent **M1** with 0.1 mM concentration in the solvent of DCM. The solution of **M1-H** is formed with 0.1 mM **M1** and 100 eq. TFA. (**B**) UV-Vis spectra of 1 mM **M1** in solvent mixture of DCM/TCB (1/4) with different equivalent of TFA added. Related to Figure 2.

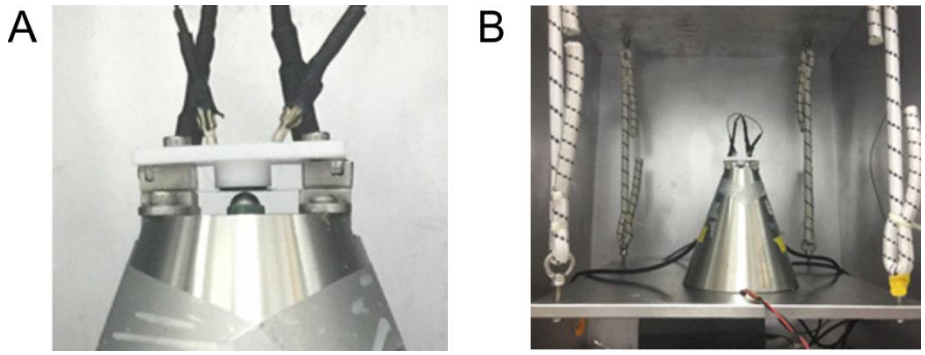

Figure S11. (**A**) Side view of the MCBJ setup. (**B**) Overview of the MCBJ setup with a suspension to damp vibration. Related to Figure 2.

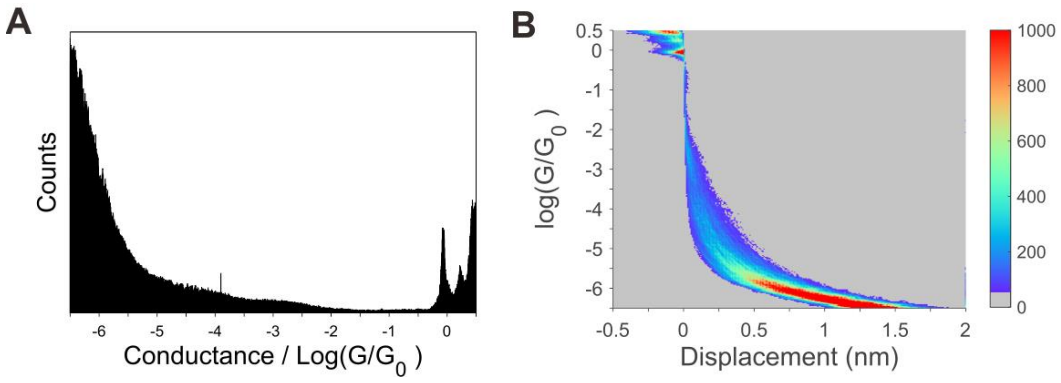

Figure S12. All data-point one-dimensional (**A**) and two-dimensional(**B**) conductance histograms constructed from two thousand MCBJ traces for the solvent DCM/TCB (*v*/*v*,1/4). The above measurements were perform at room temperature with 0.10 V bias applied. Related to Figure 2.

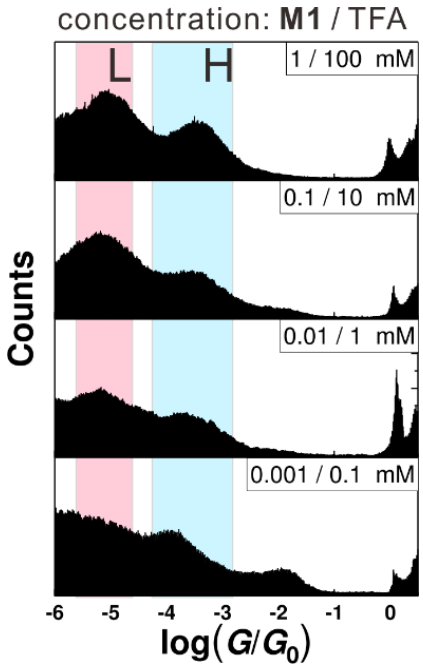

Figure S13. The one-dimensional conductance histograms by varying the concentrations between **M1** and TFA (with the ratio of 1/100). Related to Figure 2.

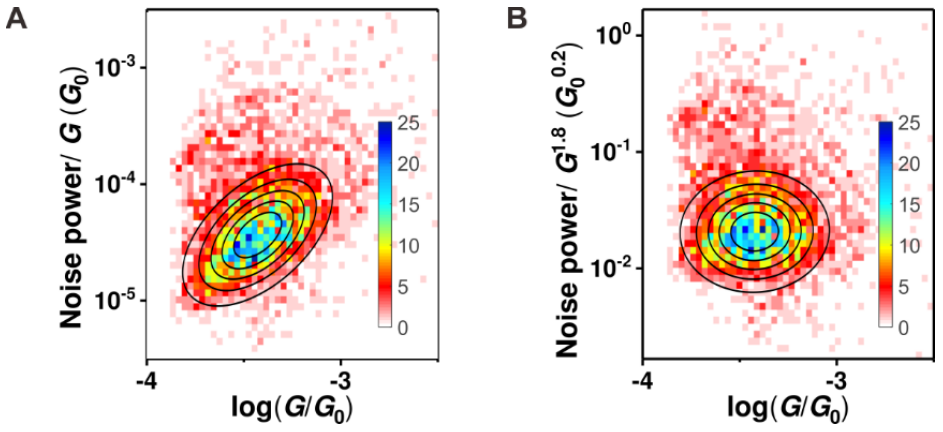

Figure S14. Two-dimensional histogram of normalized flicker noise power versus average conductance for the high-conductance junctions of **M1-H** normalized by $G^{1.0}$ (**A**), and normalized by $G^{1.8}$ (**B**). Related to Figure 2.

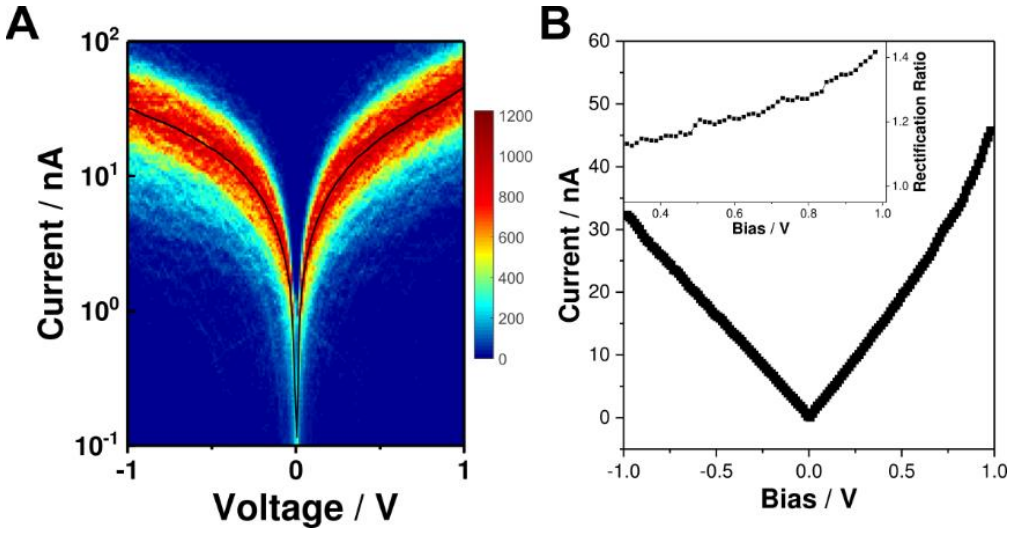

Figure S15. (**A**) The two-dimensional *I*/*V* histogram for **M1-H** constructed from about 2000 traces. The I/V histogram is fitted by Gaussian distribution shown by the black solid line. (**B**) The linear histogram for the fitted I/V character with the rectification ratio shown inset. Related to Figure 2.

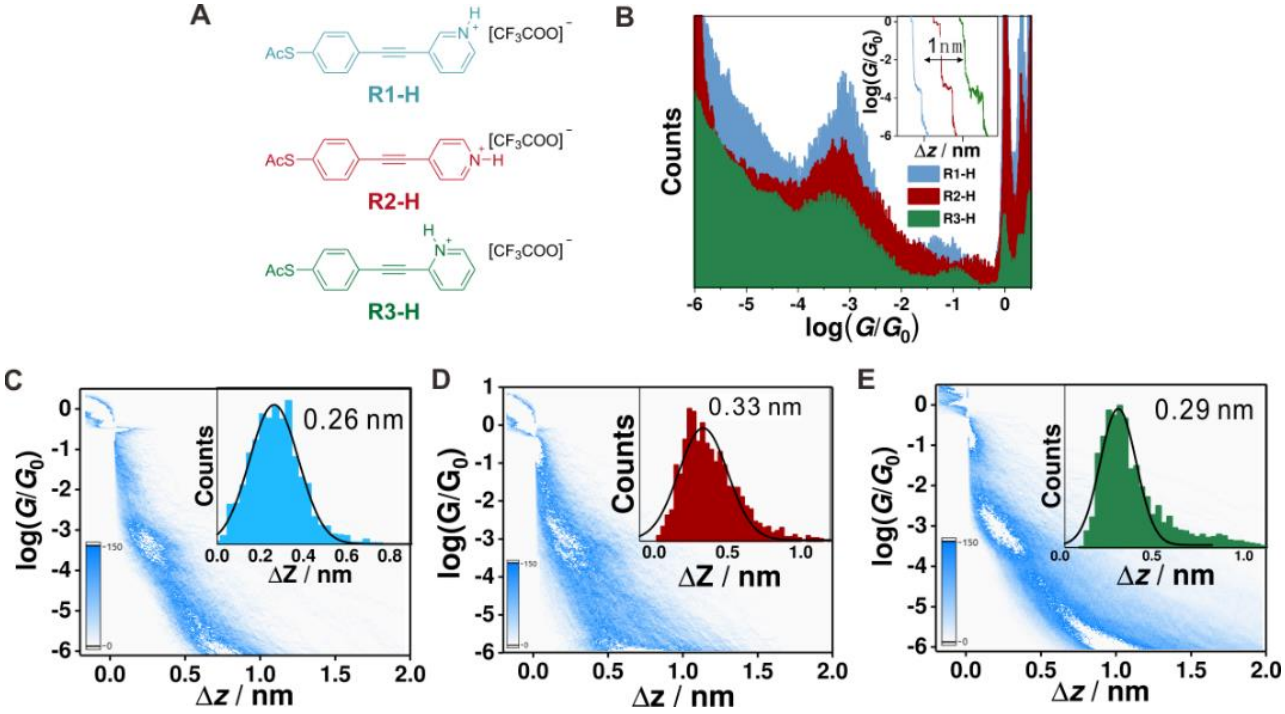

Figure S16. (**A**) Molecular structures of reference molecules. (**B**) All data-point one-dimensional conductance histograms constructed from about two thousand conductance traces. (**C**-**E**) Two-dimensional conductance histograms of **R1-H** (**C**), **R2-H** (**D**) and **R3-H** (**E**) with stretching distance Δ*z* distributions shown inset. Related to Figure 2.

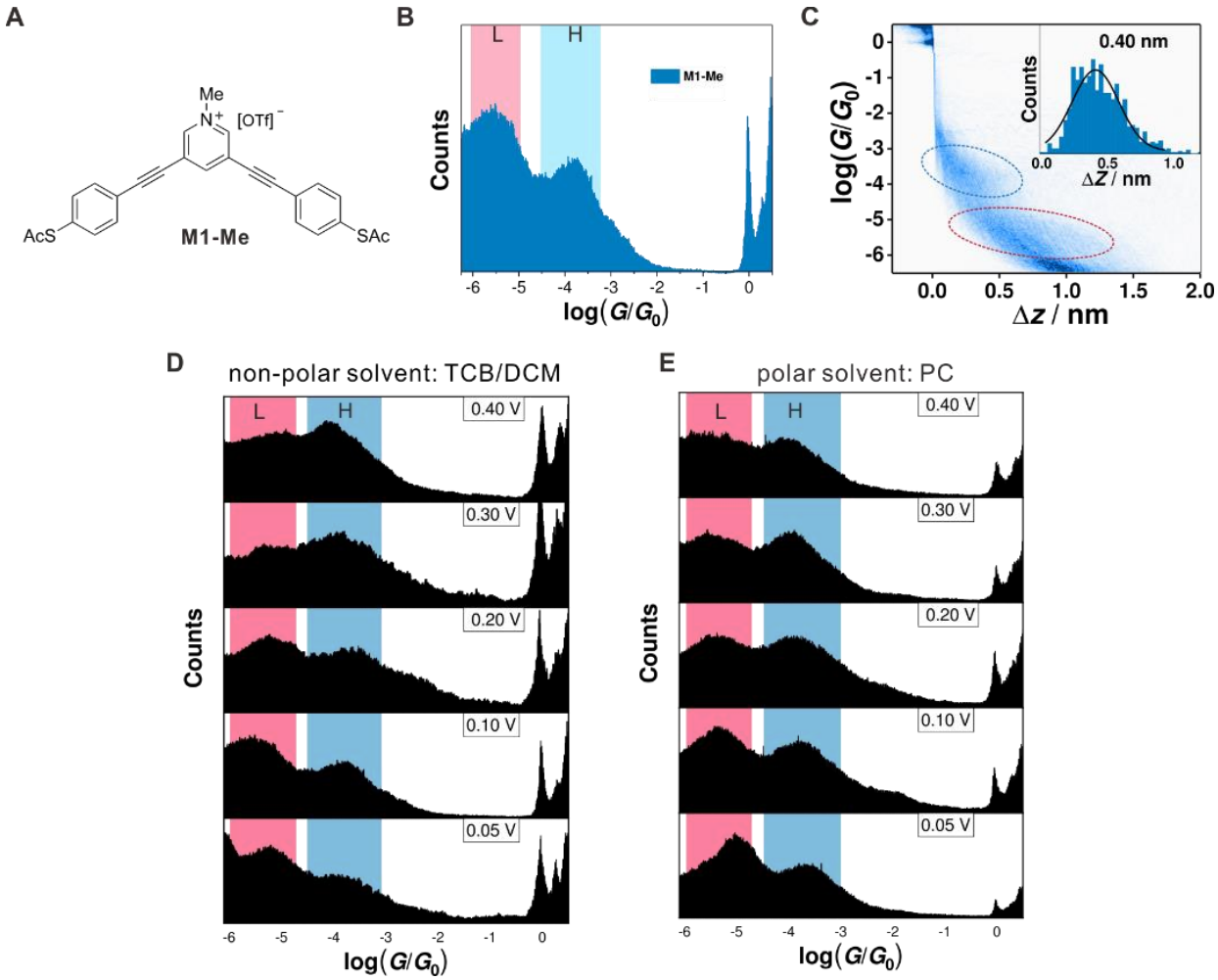

Figure S17. (**A**) Molecular structures of **M1-Me**. (**B**) All data-point one-dimensional conductance histograms constructed from about two thousand conductance traces. (**C**) Two-dimensional conductance histograms of **M1-Me** with stretching distance Δz distributions shown inset. (**D**) One-dimensional conductance histograms of **M1-Me** with a different bias applied, in the solvent TCB/DCM mixture (*v*/*v*, 4/1). (**E**) One-dimensional conductance histograms of **M1-Me** with a different bias applied, in the solvent of propylene carbonate (PC). Related to Figure 2 and Figure 3.

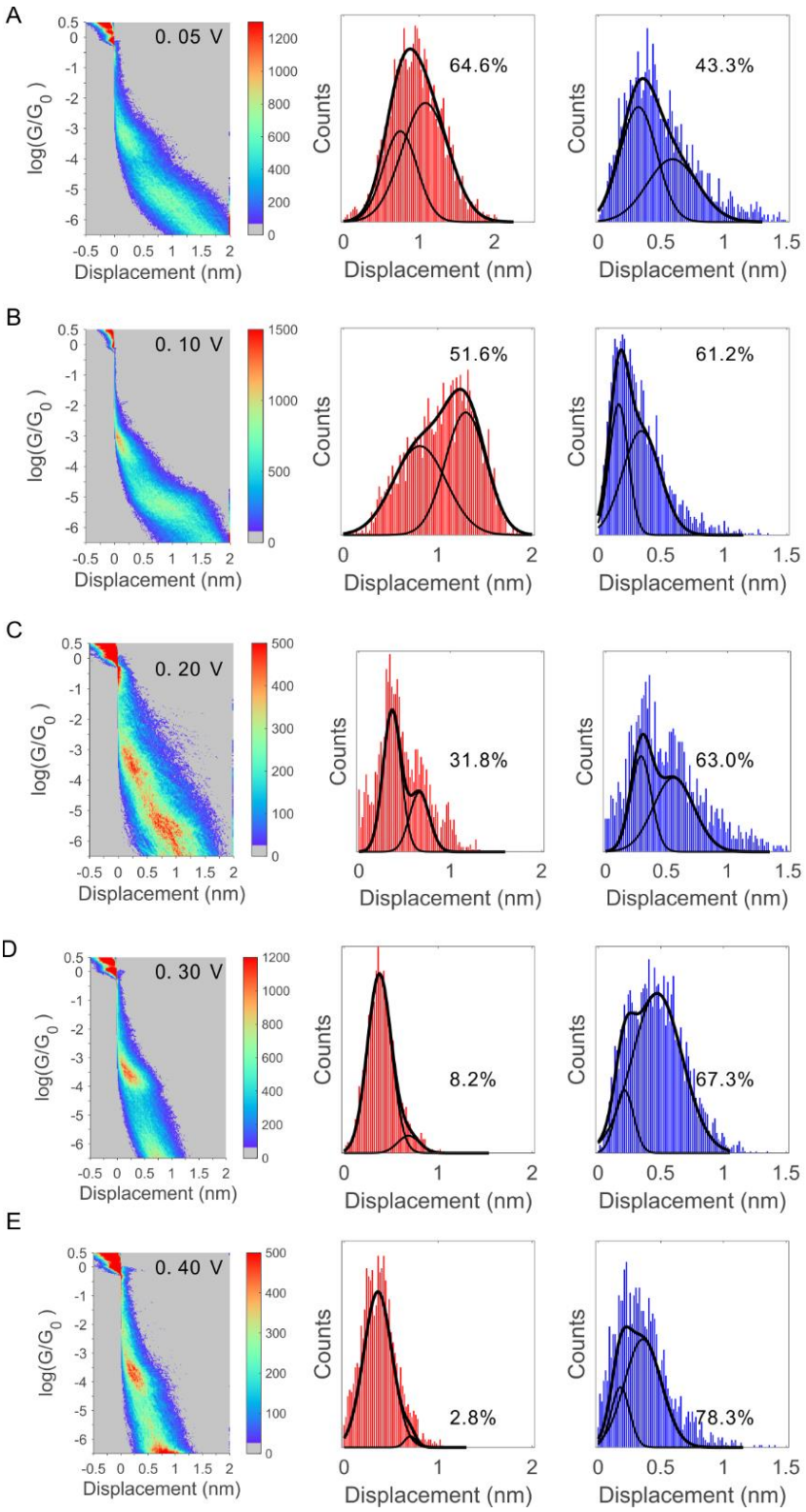

Figure S18. 2D conductance histogram of **M1-H** in the bias of 0.05 (a), 0.10 (b), 0.20 (c), 0.30 (d), and 0.40 V (e) respectively. Junction formation probability analyzing for the low conductance regions are shown in the middle panels, while that for the low conductance regions are shown in the right panels. Related to Figure 3A.

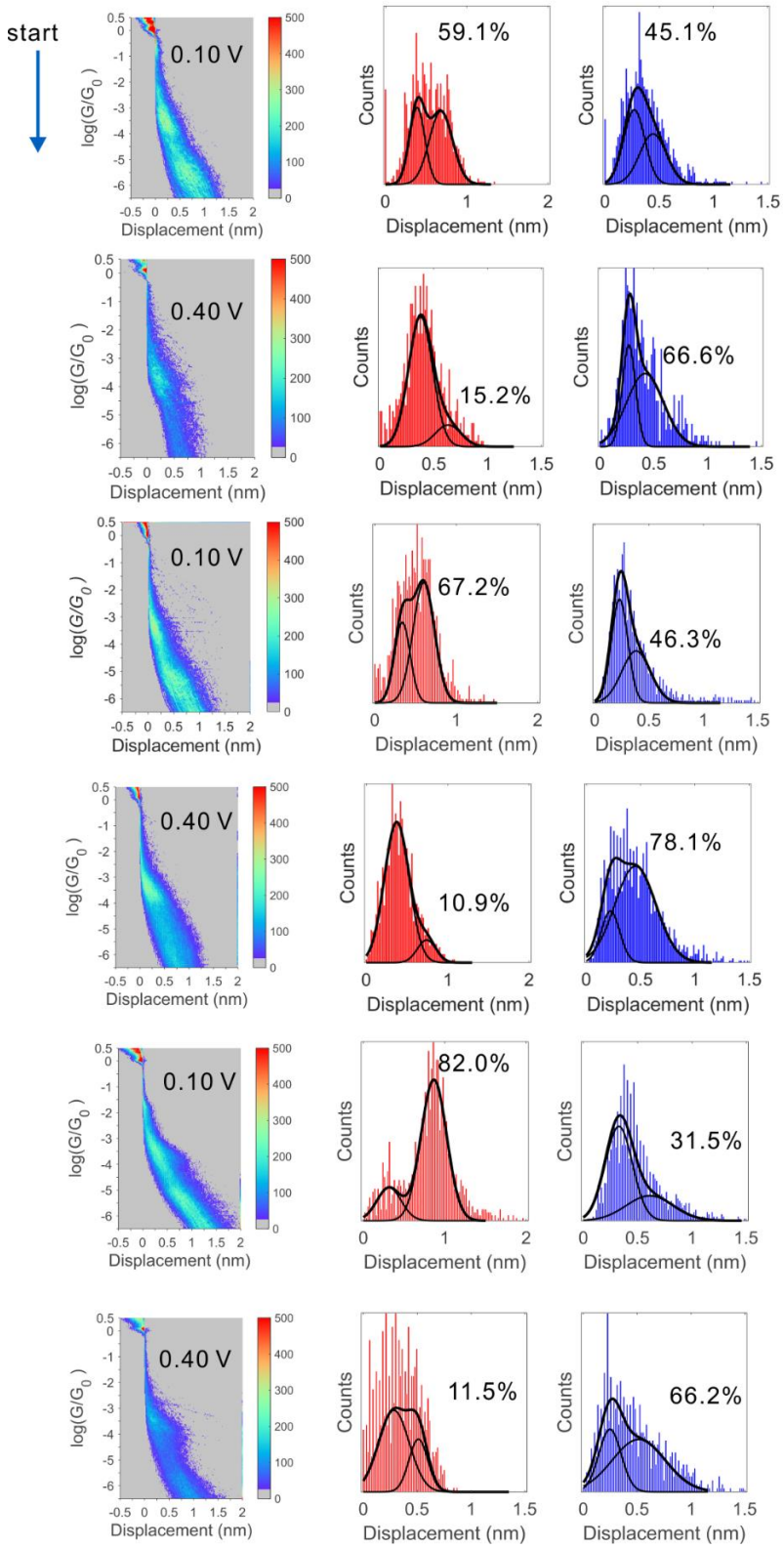

Figure S19. 2D conductance histogram (left panel) of **M1-H**. Junction formation probability analyzing for the low- and high-conductance regions are shown in the middle and right panels. Related to Figure 3D.

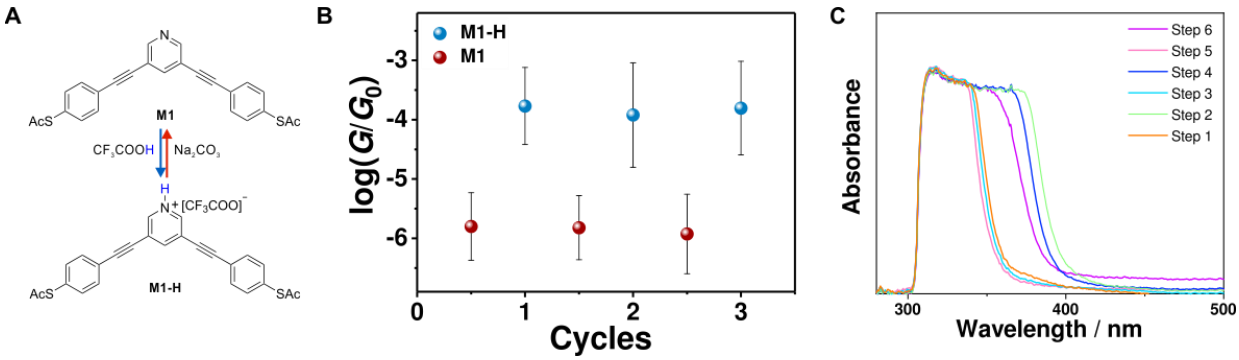

Figure S20. (**A**) The structures of **M1-H** and **M1**, which show reversible switching with base or acid added. (**B**) Reversible switching of molecular conductance between **M1-H** and **M1** with acid or base treatment successively. The MCBJ experiments were performed under a solvent mixture (DCM/TCB = 1/4) with 0.10 V bias applied. The reversibility between **M1** and **M1-H** was accomplished as mentioned above. (**C**) UV-Vis spectra of the layer of solvent mixture (DCM/TCB = 1/4) in each cycle step. Related to Figure 2.

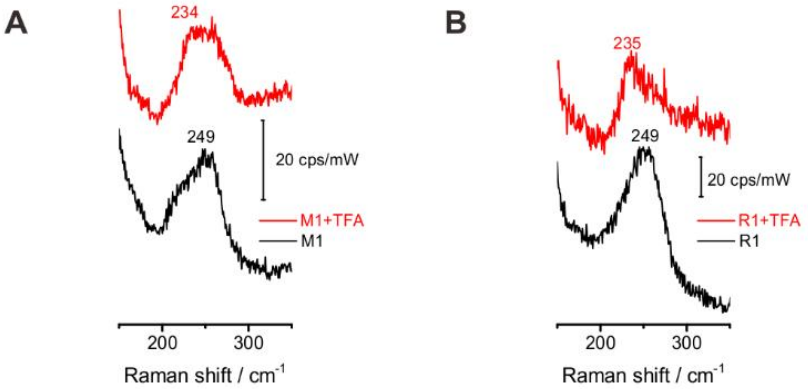

Figure S21. Surface enhance Raman spectra. **M1**/ **M1-H** (**A**) and **R1**/ **R1-H** (**B**) on gold nanoparticles. Related to Figure 4E.

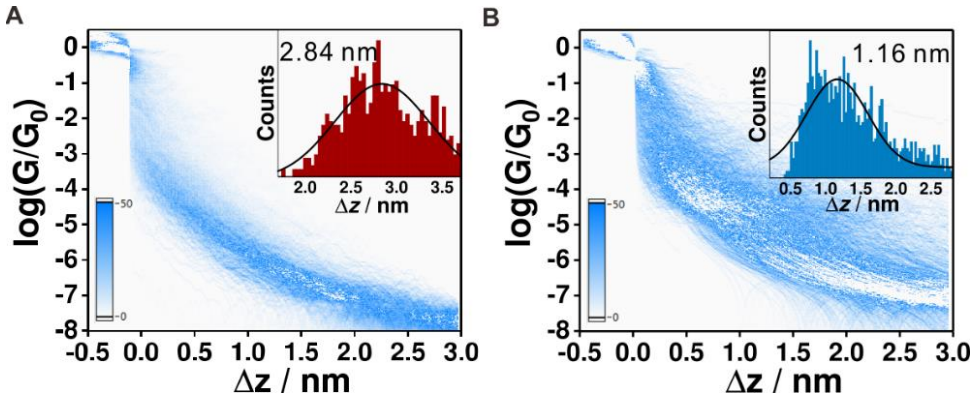

Figure S22 Two-dimensional conductance histograms of **M1L** (**A**) and **M1L-H** (**B**) with stretching distance Δ*z* distributions shown inset. It is worth noting that the most probable conductance for the low-conductance junctions of **M1L** is lower than $10^{-7.1}$ G_0, which is below the detecting limit of our devices. Only 15% single traces of **M1L** show molecular platitudes, leading to the molecular peak centered at $10^{-7.1}$ G_0, which is the distribution of the high value area. We also tried to measure the low-conductance junction of **M1L-H**, but the background noise ($10^{-7.0}$ G_0) is alway higher that the measurement in neutral state **M1L**, thus we think the low-conductance junctions of **M1L-H** should below $10^{-7.0}$ G_0. We found that the molecules similar to **M1L** with *para*-connectivity has a conductance centered at $10^{-7.0}$ G_0, which means the most probable conductance for corresponding molecules in *meta*-connectivity should below $10^{-8.0}$ G_0. We actually underestimate the conductance difference between the two connectivities of **M1L-H**, which should have far more conductance difference than 400 times. Related to Figure 2.

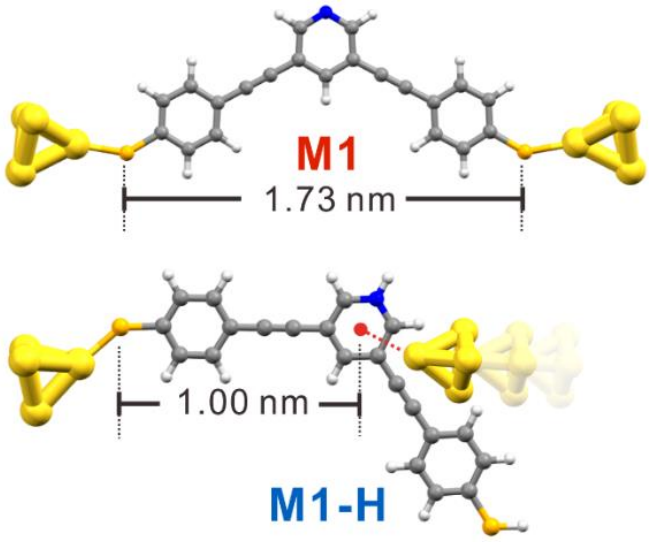

Figure S23. The end-to-end connectivity for **M1** (top), and the in-backbone connectivity for **M1-H** (bottom), with theoretical lengths 1.73 and 1.00 nm respectively. Related to Figure 2.

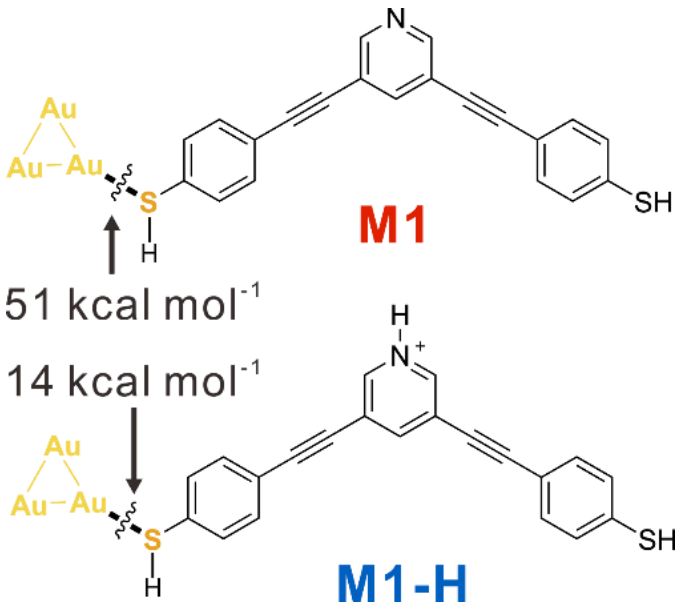

Figure S24. The Au←SH coordination bond formation energy of **M1** and **M1-H.** Related to Figure 4E.

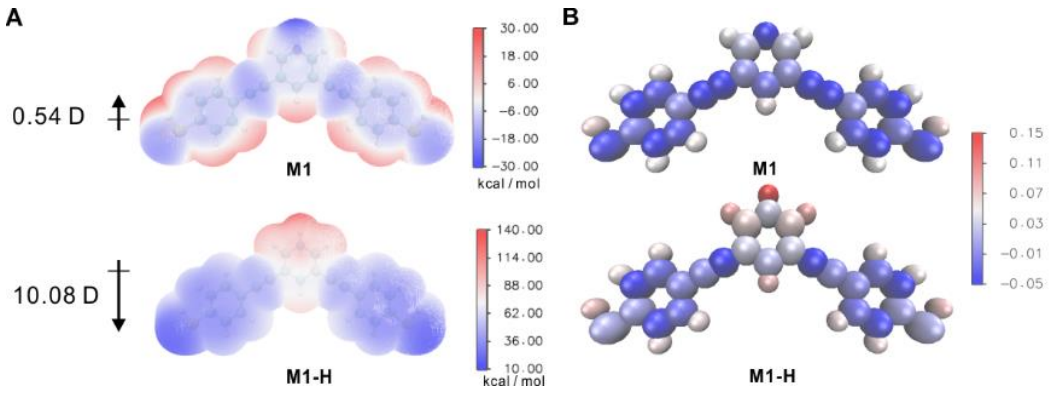

Figure S25. (**A**) The electrostatic potential distributions of **M1** and **M1-H**, with their dipole moments shown by the arrows. (**B**) The atomic charge distribution of **M1** and **M1-H**. Related to Figure 4.

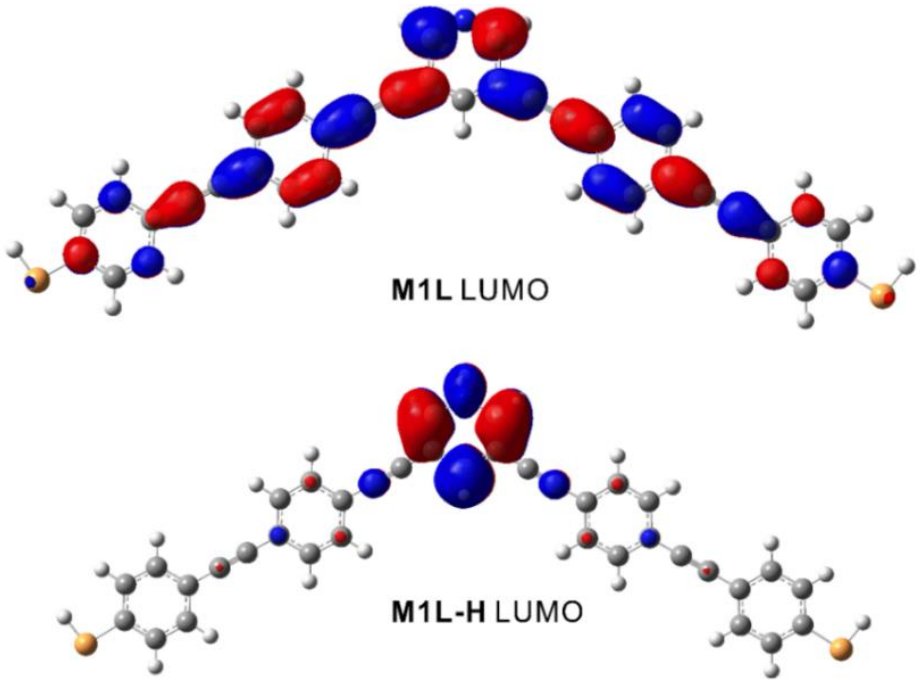

Figure S26. The upper panel is the LUMO of **M1L** and the bottom panel is the LUMO of **M1L-H**. Related to Figure 4.

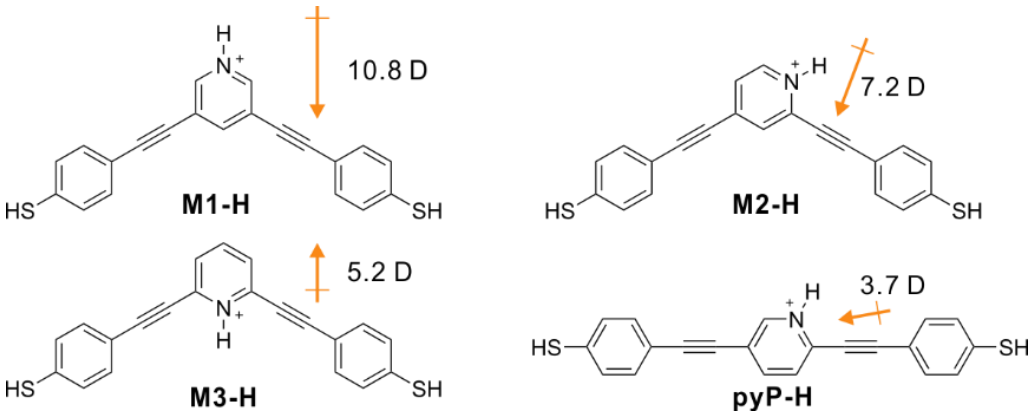

Figure S27. The strength and direction of the dipole moments of the protonated pyridiniums with nitrogen in different positions. Related to Figure 4.

Transparent Methods

Section 1. Synthesis and Characterization

General Information.

Commercially available reagents and solvents obtained from chemical suppliers were used without further purification unless otherwise noted. Nuclear magnetic resonance (NMR) spectroscopic experiments were performed on Bruker AV–500 spectrometers (400 MHz). ^{1}H NMR spectra were recorded at 400 MHz and chemical shifts are reported in ppm using residual deuterated solvent peak as reference ($CDCl_3$: δ 7.26, CD_2Cl_2: δ 5.30). The following abbreviations were used to explain the multiplicities: s = singlet, d = doublet, t = triplet, q = quartet, m = multiplet, br = broad. ^{13}C NMR spectra were recorded at 100 MHz using broadband proton decoupling and chemical shifts are reported in ppm relative to residual deuterated solvent peak ($CDCl_3$: δ 77.00). High-resolution mass spectra (HRMS) experiments were recorded on a Bruker En Apex Ultra 7.0T Fourier Transform Mass Spectrometer.

Preparation and characterization

Compound **M1**, **R1**, **R2,** and **R3** were synthesized according to the previous results(Liu et al., 2017b). Compound **M1L** was synthesized with similar protocol.

To characterized the NMR of **M1-H** and reduce the interference of TFA, we added 5 eq. TFA to the solution ($CDCl_3$) of **M1**, leading to the formation of **M1-H** in-situ.

Characterization of compound **M1-H**: ^{1}H NMR (400 MHz, $CDCl_3$): δ = 8.82 (br, 2H), 8.39 (s, 1H), 7.52 (t, J = 8.52 Hz, 4H), 7.37 (t, J = 8.50 Hz, 4H), and 2.37 (s, 6H). ^{13}C NMR (100 MHz, CD_2Cl_2): δ = 194.05, 159.61, 147.56, 142.97, 134.45, 132.66, 130.70, 121.60, 97.87, 82.57 and 30.38. HRMS (ESI): *m/z* calcd for $[C_{25}H_{18}NO_2S_2]^+$, 428.0773 ; found, 428.0735.

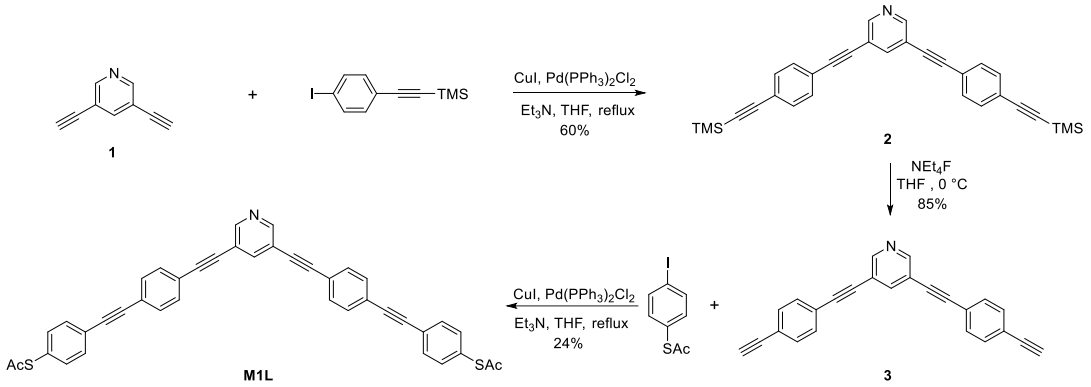

Figure S28. The synthetic route of **M1L**.

3,5-bis((4-((trimethylsilyl)ethynyl)phenyl)ethynyl)pyridine (Compound **2**): To a solution of 3,5-diethynylpyridine (200 mg, 1.57 mmol, 1 equiv.), ((4-iodophenyl)ethynyl)trimethylsilane (992 mg, 3.30 mmol, 2.1 equiv.) and 10 mL degassed Et_3N in 20.0 mL of anhydrous THF were added $Pd(PPh_3)_2Cl_2$ (56 mg, 0.08 mmol, 0.05 equiv.) and CuI (30 mg, 0.16 mmol, 0.1 equiv.) under an N_2 atmosphere. The reaction mixture was refluxed for 8 hours and then cooled to room temperature. Saturated ammonium chloride (10mL) was added, the resulting mixture was extracted with Et_2O (2 x 20 mL). The combined organic solution was washed with brine (20 mL), dried over anhydrous $MgSO_4$, filtered and concentrated under reduced pressure. The residue was purified by flash column chromatography to give compound 2 in 60% yield.

Characterization of compound **2**: Pale yellow solid. ^{1}H NMR (500 MHz, $CDCl_3$) δ 8.672 (d, J = 1.9 Hz, 2H), 7.914 (t, *J* = 1.9 Hz, 1H), 7.469 (s, 8H), 0.262 (s, 18H); ^{13}C NMR (125 MHz, $CDCl_3$) δ 150.9, 140.5, 132.0, 131.5, 123.8, 122.2, 119.9, 104.4, 96.9, 92.9, 86.9, –0.12. IR (neat, cm^{-1}): 3368, 3294, 2923, 2852, 1655, 1261, 1017, 836, 801, 750, 698, 670, 660, 428. HRMS (ESI): *m/z* calcd for $[C_{31}H_{29}NSi_2+H]^+$, 472.1911; found, 472.1935.

3,5-bis((4-ethynylphenyl)ethynyl)pyridine (compound **3**): The solution of compound **2** (200 g, 0.42 mmol) in THF (50mL) was added tetrabutylammonium fluoride (0.42 mmol, 1 M in THF) at 0 °C. The mixture was stirred for 15 min and saturated ammonium chloride (10mL) was added. The resulting mixture was extracted with Et_2O (2 x 20 mL). The combined organic solution was washed with brine (20 mL), dried over anhydrous $MgSO_4$,

filtered and concentrated under reduced pressure. The residue was chromatographed to give compound **3** in 85% yield.

Characterization of compound **3**: Brown solid. ^{1}H NMR (500 MHz, $CDCl_3$) δ 8.685 (s, 2H), 7.934 (s, 1H), 7.496 (s, 8H), 3.202 (s, 2H); ^{13}C NMR (125 MHz, $CDCl_3$) δ 151.0, 140.6, 132.2, 131.6, 122.8, 122.7, 119.9, 92.7, 87.0, 83.0, 79.3. IR (neat, cm^{-1}): 3358, 3206, 3029, 2957, 2922, 2851, 2155, 1633, 1259, 1134, 1087, 865, 836, 801, 698, 636, 485, 449. HRMS (ESI): *m/z* calcd for $[C_{25}H_{13}N+H]^+$, 328.1121; found, 328.1128.

S,S'-((((pyridine-3,5-diylbis(ethyne-2,1-diyl))bis(4,1-phenylene))bis(ethyne-2,1-diyl))bis(4,1-phenylene)) (compound **M1L**): To a solution of compound **3** (100 mg, 0.30 mmol, 1 equiv.), S-(4-iodophenyl) ethanethioate (175 mg, 0.63 mmol, 2.1 equiv.) and 5 mL degassed Et_3N in 10.0 mL of anhydrous THF were added $Pd(PPh_3)_2Cl_2$ (9 mg, 0.015 mmol, 0.05 equiv.) and CuI (5 mg, 0.16 mmol, 0.1 equiv.) under an **N_2** atmosphere. The reaction mixture was refluxed for 24 hours and then cooled to room temperature. Saturated ammonium chloride (10mL) was added, the resulting mixture was extracted with Et_2O (2 x 20 mL). The combined organic solution was washed with brine (20 mL), dried over anhydrous $MgSO_4$, filtered and concentrated under reduced pressure. The residue was purified by flash column chromatography to give compound **M1L** in 24% yield.

Characterization of compound **M1L**: Pale yellow solid. ^{1}H NMR (500 MHz, CD_2Cl_2) δ 8.676 (s, 2H), 7.953 (s, 1H), 7.53–7.58 (m, 12H), 7.412 (d, J = 8.0, 4H), 2.409 (s, 6H); owing to poor solubility of **M1L**, its ^{13}C NMR is difficult to be characterized. IR (neat, cm^{-1}): 3367, 2960, 2922, 2852, 1655, 1262, 1084, 1015, 837, 827, 796, 729, 696, 670, 636, 599, 554, 424. HRMS (ESI): *m/z* calcd for $[C_{41}H_{25}NO_2S_2+H]^+$, 628.1399; found, 628.1419

3,5-bis((4-(acetylthio)phenyl)ethynyl)-1-methylpyridin-1-ium trifluoromethanesulfonate (compound **M1-Me**): A mixture of compound **M1** (50 mg, 0.12 mmol) and methyl trifluoromethanesulfonate (30 mg, 0.18 mmol) in 10 mL diethyl ether was stirred at RT for 15 min to give a yellow precipitate, and then the precipitate was isolated by filtration. Further recrystallizing from the mixed solvent (DCM/Et_2O, 10/1) and evaporating under vacuum to give a pale yellow solid. Yield, 55 mg, 79%.

Characterization of compound **M1-Me**: Pale yellow solid, 79% yield. ^{1}H NMR (400 MHz, $CDCl_3$): δ = 8.86 (s, 2H), 8.49 (s, 1H), 7.63 (d, J = 8.29 Hz, 4H), 7.47 (d, J = 8.29 Hz, 4H), 4.43 (s, 3H) and 2.45 (s, 6H). ^{13}C NMR (100 MHz, CD_2Cl_2): δ = 193.10, 147.55, 145.51, 134.48, 132.66, 131.49, 125.03, 121.38, 98.12, 82.57, 49.19 and 30.25. IR (neat, cm^{-1}): 3369, 2923, 2853, 2218, 1658, 1632, 1467, 1412, 1350, 1265, 1084, 1031, 946, 897, 736, 700, 511. HRMS (ESI): *m/z* calcd for $[C_{26}H_{20}NO_2S_2]^+$, 442.0930; found, 442.0931.

Section 2. MCBJ Experimental Methods

Home-made MCBJ setup

As shown in Figure S11, our home-made MCBJ setup was used to measure the molecular conductance between two gold electrodes. During the MCBJ measurement, a sheet of steel was taken as substrate and fixed by two supports on both ends. The notched gold wire and liquid cell were fixed upon the substrate. The pushing rod below the substrate was used to bend and release the substrate repeatedly, resulting in the repeating breaking and re-connecting of gold wire. To have precise control, a piezo actuator was used as the pushing rod. During the repeating breaking and re-connecting operation, the real-time conductance was recorded by the home-built *I*-*V* converter.

Single-molecule conductance measurement

Conductance measurements were performed in solution at room temperature with our home-built MCBJ setup (Li et al., 2017). We used two kinds of solutions: a mixture of dichloromethane (DCM) / trichlorobenzene (TCB) (*v*/*v*: 1 / 4); pure propylene carbonate (PC). Protonated pyridiniums **M1-H**, **R1-H**, **R2-H**, **R3-H**, and **M1L-H** were in-situ formed according to published protocol (Boyle et al., 2017). The methylated pyridinium **M1-Me** are directly dissolved in corresponding solutions. In both solutions, we dissolved 1 mM of target molecules for the following characterizations. During the MCBJ measurement, a spring steel sheet was taken as substrate and fixed by two supports on both ends. The notched gold wire and liquid cell were fixed upon the substrate. The real-time conductance was recorded by the home-built *I*-*V* converter with a sampling rate of 20 *k*Hz. For each experiment, more than one thousand conductance traces were recorded for statistical analysis.

Data analysis

In the measurement of single-molecule conductance, since the variation of molecular junction configuration results the variation of conductance, in each experiment, we record thousands of individual single traces, and apply a statistical approach to determine the most probable conductance and the stretching distance.

The conductance traces without forming molecular junctions were excluded for analysis as reported in our previous paper (Hong et al., 2012, Huang et al., 2015, Liu et al., 2017a). One-dimensional conductance histograms were constructed by collecting all individual traces with a bin size of 1100 for $\log(G/G_0)$ from –10 to +1, and 1000 for Δz from –0.5 to 3 nm. The conductance distribution was extracted by calculating the data density in each bin. The peak shift in a conductance histogram was determined by Gaussian fitting, which represents the most probable molecular conductance.

2D conductance-displacement histograms were plotted by overlapping each individual trace with a bin size of 1100 for $\log(G/G_0)$ from –10 to +1, and 1000 for Δz from –0.5 to 3 nm. All traces are aligned with a relative zero point ($\Delta z = 0$) at $G = 0.5\ G_0$. Then the 2D conductance distribution versus the relative distance was constructed by the data counts in each bin.

To construct the displacement distribution histograms, firstly the relative stretching distance, Δz, was determined from the position where the conductance is $0.5\ G_0$ (after the rupture of the gold-gold atomic break at G_0), to the molecular conductance region, just before the end of the molecular plateau. The peak represents the most probable plateau length. To find the absolute displacement, z^*, which is related to the most probable length of the molecular junction, the relative displacements were corrected by adding the snap-back distance, Δz_{corr}, to the relative displacement Δz, namely, $z^* = \Delta z + \Delta z_{corr}$. Referring to the previous result[3], Δz_{corr} was determined experimentally to be 0.5 ± 0.1 nm.

Evaluation of the concentration effect

When we change both the concentration of **M1** and TFA in MCBJ measurements (Figure S13), we find that the concentration chaning leads to the variation of junction formation probability for both connectivities. So that in our experiments, we use a relatively higher concentration (1.0 mM) to ensure high junction formation probability for both two connectivities.

Section 3. Junction Geometry Analyzing

Flicker noise analysing for the high-conductance junctions of M1-H

To probe the junction geometry, we performed flicker noise analysis on the high-conductance junction of **M1-H**. According to previous reports, the flicker noise of the single-molecule junctions reflects the coupling between electrodes and molecules (Adak et al., 2015, Garner et al., 2018). The noise power of through-space coupling scales as $G^{2.0}$, where G is the mean conductance. It is in contrast to the through-bond coupling, where the noise power scales as $G^{1.0}$. We paused the junction elongation process at the high-conductance region of **M1-H** for 150 ms, during which time the conductance signals were extracted out for noise analysis. As shown in Figure S14A, when the noise power is normalized by $G^{1.0}$, we find a positive correlation between the noise power and average conductance, and such correlation is minimized when the noise power normalized by $G^{1.8}$ (Figure S14B). Such correlation suggests a junction geometry of through-space coupling, which is consistent with the ring coupling of pyridinium to the gold electrode.

I/V characterization for the high-conductance junctions of M1-H

The I/V characterization was performed as the following: once a molecule junction was formed during the stretching process, we suspended the stretching process and applied a voltage ramp between -1 and 1 V. The ring coupling of **M1-H** would lead to an asymmetric junction geometry, which was verified by the I/V characterization, showing a moderately asymmetric character with a rectification ratio of ~1.5 (Figure S15).

Evaluating the bonding energy of Au-S through Surface enhance Raman spectra

The 0.1mM solution of target molecules in THF were dropped on the gold substrate to form molecule assembly and the gold nanoparticles dispersed in water were dropped and dried under vacuum by the water pump to form a ‘coffee ring’ pattern. The SERS spectra were collected at IDSpec Arctic system under 50X-long working

distance objective lens. The protonation was performed by adding 100 eq. TFA into the THF solution of target molecules, which were used for SERS characterization as mentioned above.

Characterization of reference molecules with one –SAc anchor

We characterized the single-molecule conductance of other pyridiniums **R1-H** (Figure S16A) with only –SAc group. We observe the formation of molecule junctions in the 1-D conductance histogram of **R1-H** (Figure S16B). The molecular conductance peak of **R1-H** centers at $10^{-3.2}$ G_0, which is distinct to the neutral state of **R1-H** with a conductance peak centers at $10^{-3.9}$ (Liu et al., 2017b). Meanwhile, **R1-H** shows a similar stretching pattern (Figure S16C) to **M1-H** with about 0.31 nm stretching distance. By characterizing another two reference molecules similar to **R1-H** with nitrogen set in different positions (Supplementary Figure S16), we also observe similar conductance and stretching patterns.

M1-Me (Figure S17A) is also able to form molecular junctions, with a molecular conductance of $10^{-3.6}$ G_0 (Figure S17B) and 0.35 nm junction stretching distance (Figure S17C), both of which is similar to **M1-H**.

Section 4. Reversible Switching

Calculating the junction formation probability of M1-H in different bias

By increasing the bias from 0.05 to 0.40 V gradually, we recorded about 2000 conductance traces of **M1-H** without data selection. As shown in Figure S18, we applied double peaks Gaussian fitting to both the high- and low-conductance junction, the corresponding junction formation probability are shown beside.

Reversible changing the junction formation of M1-H by switching the bias between 0.10 and 0.40 V

By varying the bias between 0.10 and 0.40 V alternatively, we recorded about 1000 conductance traces of **M1-H** without data selection. As shown in Figure S19, we applied double peaks Gaussian fitting to both the high- and low-conductance junction, the corresponding junction formation probability are shown beside.

The acid-base pair of M1 and M1-H with reversible conductance transformation

The MCBJ conductance measurement was firstly performed on the 1 mM solution (DCM/TCB = 1/4) of **M1**. After collecting more than one thousand conductance traces, the solution in the MCBJ setup was took out. Then 100 eq. TFA was added into the 0.1 mM solution of **M1**, and 50 μL of the mixed solution was put in the same MCBJ setup and the conductance traces were also collected for more than one thousand**.** The neutral pyridine was reproduced by the treatment of Na_2CO_3 aqueous solution (2.0 M) to the equal volume solution of **M1-H** (the mixed solution just formed), after mixing the solutions and stewing for stratification, the organic layer was taken out for conductance measurements. Circularly, this organic solution is treated again with TFA and Na_2CO_3 sequentially and all the single-molecule conductance measurements in each repetitive process are characterized with at least one thousand traces.

Section 5. Theoretical Calculation

Geometry optimizing for calculating junction lengths

It's worth noting that in the above experiment, especially in the acid condition, the thioacetates would be easily deprotonated at the gold surface (Lau et al., 2006), we used actually the deprotected analogies of **M1**, **M1-H**, **M1L** and **M1L-H** for the following calculations. All the calculations were performed with the Gaussian 09 software package(Frisch et al., 2013). The B3LYP/6-311++G(d,p)(Becke, 1993, Ernzerhof and Scuseria, 1999) level of density functional theory was used to optimize all of the structures for **M1** and **M1L** and the cation of **M1-H** and **M1L-H**. The theoretical junction lengths were calculated by the distance between two thiol groups or between one of the thiol and the middle point of pyridine rings.

Evaluating the bonding energy of Au-S

To evaluate bonding energy, the models were optimized by PBE0(Hay and Wadt, 1985a, b) method including dispersion correction (DFT-D3) (Grimme et al., 2010). Standard basic set 6-311G(d,p) was used to describe C, N, H and S atoms, and the effective core potentials. Lanl2TZ(f) was used to describe the effective core potential of Au(Hay and Wadt, 1985a, b, Wadt and Hay, 1985).

There are three effects to weaken the Au-S bond. Firstly, the Au-S covalent bond and Au←SH coordination bond will both be possible existing in the gold surface (Inkpen et al., 2019). And the **M1-H** is formed in situ from the acidic environment, which will inhibit the deprotonation of –SH, and facilitate the formation of Au←SH coordination bonds, with significantly weaker bonding energy (Figure S24). Secondly, according to hard/soft acid/base principles, gold is soft acid, which will have a stronger interaction with more polarizable atom. From the atomic charge distribution (Figure S26), the negative charge of sulfur atoms in **M1-H** is obviously smaller than that in **M1**, so that the sulfur atoms in **M1** is more polarizable than that in **M1-H**, which will lead to different bonding energy between them. Thirdly, the LUMO of **M1-H** is localized in the pyridinium ring, and thiol atoms show almost none distribution at the thiol atoms in the LUMO **M1-H**. While the LUMO of **M1** shows a delocalized pattern, the non-hybridized p orbital of the thiol atoms can conjugate with the π system, which will facilitate the back donation from the d orbital of golds to the p orbitals of thiols. The enhanced back donation will also lead to stronger Au-S bonding energy in **M1** than that in **M1-H**.

The effect of EEF on total electronic energy

To evaluate the effect of EEF, the models used to evaluate Au-S formation energy (Figure S24) were used to study their total electronic energy changes by altering the strength and orientation of EEF. The applied EEF was along the z-axis with the strength changing from –0.006 to +0.006 a.u., and the strength was fixed at +0.006 a.u with molecule orientation changed from -90^{o} to 90^{o}. Then all the models were optimized by PBE0 method including dispersion correction (DFT-D3) (Grimme et al., 2010). Standard basic set 6–311G(d,p) was used to describe C, N, H and S atoms, and the effective core potentials. Lanl2TZ(f) was used to describe the effective core potential of Au(Hay and Wadt, 1985a, b, Wadt and Hay, 1985).

Supplemental References

Adak, O., Rosenthal, E., Meisner, J., Andrade, E.F., Pasupathy, A.N., Nuckolls, C., Hybertsen, M.S., and Venkataraman, L. (2015). Flicker noise as a probe of electronic interaction at metal–single molecule interfaces. Nano Lett. 15, 4143-4149.

Becke, A.D. (1993). Density‐functional thermochemistry. Iii. The role of exact exchange. J. Chem. Phys. 98, 5648-5652.

Boyle, T.J., Yonemoto, D.T., Sears, J.M., Treadwell, L.J., Bell, N.S., Cramer, R.E., Neville, M.L., Stillman, G.A.K., and Bingham, S.P. (2017). Synthesis, characterization, and utility of trifluoroacetic acid lanthanide precursors for production of varied phase fluorinated lanthanide nanomaterials. Polyhedron 131, 59-73.

Ernzerhof, M., and Scuseria, G.E. (1999). Assessment of the perdew–burke–ernzerhof exchange-correlation functional. J. Chem. Phys. 110, 5029-5036.

Frisch, M., Trucks, G., Schlegel, H.B., Scuseria, G., Robb, M., Cheeseman, J., Scalmani, G., Barone, V., Mennucci, B., and Petersson, G. (2013). Gaussian 09, revision d. 01 (Gaussian, Inc., Wallingford CT).

Garner, M.H., Li, H., Chen, Y., Su, T.A., Shangguan, Z., Paley, D.W., Liu, T., Ng, F., Li, H., Xiao, S., et al. (2018). Comprehensive suppression of single-molecule conductance using destructive σ-interference. Nature 558, 415-419.

Grimme, S., Antony, J., Ehrlich, S., and Krieg, H. (2010). A consistent and accurate ab initio parametrization of density functional dispersion correction (dft-d) for the 94 elements h-pu. J. Chem. Phys. 132, 154104.

Hay, P.J., and Wadt, W.R. (1985a). Ab initio effective core potentials for molecular calculations. Potentials for k to au including the outermost core orbitals. J. Chem. Phys. 82, 299-310.

Hay, P.J., and Wadt, W.R. (1985b). Ab initio effective core potentials for molecular calculations. Potentials for the transition metal atoms sc to hg. J. Chem. Phys. 82, 270-283.

Hong, W., Manrique, D.Z., Moreno-Garcia, P., Gulcur, M., Mishchenko, A., Lambert, C.J., Bryce, M.R., and Wandlowski, T. (2012). Single molecular conductance of tolanes: Experimental and theoretical study on the junction evolution dependent on the anchoring group. J. Am. Chem. Soc. 134, 2292-2304.

Huang, C., Rudnev, A.V., Hong, W., and Wandlowski, T. (2015). Break junction under electrochemical gating: Testbed for single-molecule electronics. Chem. Soc. Rev. 44, 889-901.

Inkpen, M.S., Liu, Z.F., Li, H., Campos, L.M., Neaton, J.B., and Venkataraman, L. (2019). Non-chemisorbed gold–sulfur binding prevails in self-assembled monolayers. Nat. Chem. 11, 351-358.

Lau, K.H.A., Huang, C., Yakovlev, N., Chen, Z.K., and O'Shea, S.J. (2006). Direct adsorption and monolayer self-assembly of acetyl-protected dithiols. Langmuir 22, 2968-2971.

Li, R., Lu, Z., Cai, Y., Jiang, F., Tang, C., Chen, Z., Zheng, J., Pi, J., Zhang, R., Liu, J., et al. (2017). Switching of charge transport pathways via delocalization changes in single-molecule metallacycles junctions. J. Am. Chem. Soc. 139, 14344-14347.

Liu, J.Y., Zhao, X.T., Al-Galiby, Q., Huang, X.Y., Zheng, J.T., Li, R.H., Huang, C.C., Yang, Y., Shi, J., Manrique, D.Z., et al. (2017a). Radical-enhanced charge transport in single-molecule phenothiazine electrical junctions. Angew. Chem. Int. Ed. 56, 13061-13065.

Liu, X., Sangtarash, S., Reber, D., Zhang, D., Sadeghi, H., Shi, J., Xiao, Z.Y., Hong, W., Lambert, C.J., and Liu, S.X. (2017b). Gating of quantum interference in molecular junctions by heteroatom substitution. Angew. Chem. Int. Ed. 56, 173-176.

Wadt, W.R., and Hay, P.J. (1985). Ab initio effective core potentials for molecular calculations. Potentials for main group elements na to bi. J. Chem. Phys. 82, 284-298.